Observability of signatures of transport-induced chemistry in clear atmospheres of hot gas giant exoplanets

Maria Zamyatina [1]★ Eric Hébrard [1], Benjamin Drummond [2] Nathan J. Mayne [1], James Manners [2], Duncan A. Christie [1], Pascal Tremblin [3], David K. Sing [4,5] and Krisztian Kohary [1]

[1]*Department of Physics and Astronomy, Faculty of Environment, Science and Economy, University of Exeter, Exeter EX4 4QL, UK*
[2]*Met Office, Fitzroy Road, Exeter EX1 3PB, UK*
[3]*Maison de la Simulation, CEA, CNRS, Univ. Paris-Sud, UVSQ, Université Paris-Saclay, F-91191 Gif-sur-Yvette, France*
[4]*Department of Earth and Planetary Science, Johns Hopkins University, 3400 N. Charles Street, Baltimore, MD 21218, USA*
[5]*Department of Physics and Astronomy, Johns Hopkins University, 3400 N. Charles Street, Baltimore, MD 21218, USA*

ABSTRACT

Transport-induced quenching, i.e. the homogenization of chemical abundances by atmospheric advection, is thought to occur in the atmospheres of hot gas giant exoplanets. While some numerical modelling of this process exists, the three-dimensional nature of transport-induced quenching is underexplored. Here, we present results of 3D cloud- and haze-free simulations of the atmospheres of HAT-P-11b, HD 189733b, HD 209458b, and WASP-17b including coupled hydrodynamics, radiative transfer, and chemistry. Our simulations were performed with two chemical schemes: a chemical kinetics scheme, which is capable of capturing transport-induced quenching, and a simpler, more widely used chemical equilibrium scheme. We find that transport-induced quenching is predicted to occur in atmospheres of all planets in our sample; however, the extent to which it affects their synthetic spectra and phase curves varies from planet to planet. This implies that there is a 'sweet spot' for the observability of signatures of transport-induced quenching, which is controlled by the interplay between the dynamics and chemistry.

Key words: planets and satellites: atmospheres – planets and satellites: composition – planets and satellites: gaseous planets.

1 INTRODUCTION

Atmospheric characterization is one of the current top-level challenges of exoplanet science (Howell 2020). It calls for a coordinated effort by both sides of the exoplanet community, observational and theoretical, to obtain a better understanding of the exoplanets' optical structure, measured with transmission, emission and reflection spectroscopy, and phase curves (Kreidberg 2018) and simulated with a hierarchy of numerical models.

It is becoming apparent that to interpret observations of the best observational targets, currently Jovian planets in short-period orbits, or hot Jupiters, the exoplanet community requires multidimensional models that couple hydrodynamics, radiative transfer, and chemistry. Evidence of such a coupling having an impact on the observed properties of hot Jupiter atmospheres had been obtained. For example, vertical mixing was shown to cause a departure from chemical equilibrium in the atmosphere of Jupiter (Prinn & Barshay 1977) and hot Jupiter analogues (e.g. Saumon et al. 2003; Skemer et al. 2014; Zahnle & Marley 2014). Horizontal mixing, specifically prograde equatorial winds, was proven to occur in the atmospheres of HD 189733b and HD 209458b (e.g. Snellen et al. 2010; Louden & Wheatley 2015; Wyttenbach et al. 2015), and was reported to lead to departures from chemical equilibrium with 2D (e.g. Agúndez et al. 2012, 2014; Baeyens et al. 2021, 2022) and 3D forward models

(e.g. Cooper & Showman 2006; Drummond et al. 2018b, c, 2020; Mendonça et al. 2018; Steinrueck et al. 2018). 1D forward models and 1D retrievals still surpass higher dimensionality modelling in terms of computational efficiency, but do that at a cost of insufficiently capturing the 3D structure of an observed atmosphere (Irwin et al. 2020; MacDonald, Goyal & Lewis 2020; Pluriel et al. 2020).

Recently, Drummond et al. (2020) presented 3D cloud- and haze-free coupled hydrodynamics-radiation-chemistry simulations of the atmospheres of HD 189733b and HD 209458b. They showed that the choice of a chemical scheme, between the chemical equilibrium scheme (allowing pressure and temperature to affect the chemical structure) and the chemical kinetics scheme (allowing pressure, temperature, and 3D mixing to impact the chemical structure), resulted in synthetic observations from telescopes such as *JWST* (Greene et al. 2016) and *Ariel* (Tinetti et al. 2018; Charnay et al. 2022) to have potentially detectable differences between their respective simulations. Although more work is required to constrain, improve, and learn from such simulations, the results for the somewhat similar, in terms of bulk planetary parameters, HD 189733b and HD 209458b simulations showed a surprising level of sensitivity in the observable chemical composition.

In this study, we follow up on this finding, the apparent planet dependence of the observability of signatures of transport-induced chemistry, and simulate the atmospheres of two additional exoplanets with the same model and approach as in Drummond et al. (2020). To expand the explored parameter space, we choose a warm super-Neptune HAT-P-11b discovered by Bakos et al. (2010) as the smallest

★ E-mail: m.zamyatina@exeter.ac.uk

and coldest exoplanet in our sample of four exoplanets, and a hot Jupiter WASP-17b discovered by Anderson et al. (2010) as the largest and hottest exoplanet.

The outline of this paper is as follows. Section 2 introduces our model and details the parameters of our four targets. Section 3 describes the simulated HAT-P-11b, HD 189733b, HD 209458b, and WASP-17b atmospheres and compares their dynamical (Section 3.1), thermal (Section 3.2), and chemical structure (Section 3.3), as well as their observed and synthetic transmission spectra (Section 3.4.1), emission spectra (Section 3.4.2), and phase curves (Section 3.4.3). Section 4 discusses the observability of signatures of transport-induced quenching. Section 5 states our conclusions and plans for future work.

2 METHODS

2.1 Model description

We employ an idealized configuration of the Met Office UNIFIED MODEL (UM), whose dynamical (ENDGAME, Mayne et al. 2014a, b, 2017, 2019; Wood et al. 2014), radiative (SOCRATES, Edwards 1996; Edwards & Slingo 1996; Amundsen et al. 2014, 2016, 2017), and chemical (Drummond et al. 2018a, b, c, 2020) components have been adapted, tested, and applied to study gas giant atmospheres. The dynamical core of the model uses a semi-implicit semi-Lagrangian scheme to solve the full, deep-atmosphere, non-hydrostatic equations of motion discretized horizontally on to a regular longitude–latitude Arakawa-C staggered grid and vertically on to a geometric height-based Charney–Phillips staggered grid. At the poles only the meridional component of the wind is stored, and its speed and direction are determined by a least-squares best fit to the zonal wind on the grid-row closest to the pole assuming that the wind across the pole is that of a solid-body rotation. A diffusion scheme suppresses grid-scale numerical instabilities in horizontal wind velocities in the zonal direction only, with minimal additional damping applied to vertical wind velocities near the upper boundary and no damping or frictional parametrization at the bottom boundary. The radiative transfer component of the model solves the two-stream equations, considers the absorption due to H_2O, CO, CO_2, CH_4, NH_3, HCN, Li, Na, K, Rb, Cs and collision-induced absorption due to H_2–H_2 and H_2–He using the correlated-k and equivalent extinction methods for computing k-coefficients from the ExoMol line lists (Tennyson et al. 2016; see Tables A1 and A2 for details), and includes Rayleigh scattering due to H_2 and He. Alkali metal abundances are computed from their respective monatomic/polyatomic transition boundaries using the Burrows & Sharp (1999) analytical fits, with additional smoothing applied to prevent non-continuous abundance change. We do not include TiO and VO as opacity sources because our targets' planetary effective temperatures are low enough (<1700 K) to allow us to assume TiO and VO to be rained out (Burrows & Sharp 1999; Goyal et al. 2019).

The chemical component of the model provides a selection of chemical schemes, from the most simple to the more complete, but computationally demanding: (1) analytical, (2) equilibrium, (3) relaxation, and (4) kinetics. The *analytical* chemical scheme uses the Burrows & Sharp (1999) chemical equilibrium abundance formulas for H_2O, CO, CH_4, and NH_3 (see e.g. Amundsen et al. 2016). This scheme provides the most computationally efficient way of calculating H_2O, CO, CH_4, N_2, and NH_3 mole fractions, but assumes (a) H_2-dominated atmosphere with roughly solar elemental abundances, (b) all C exists in CO and CH_4, all O is in CO and H_2O, and all N is in N_2 and NH_3, (c) the interconversion between these

species is defined by two net reactions $CO + 3H_2 \rightleftharpoons CH_4 + H_2O$ and $N_2 + 3H_2 \rightleftharpoons 2NH_3$, which make this scheme (d) not applicable under H_2 dissociation (>2500 K) or low pressures. The chemical *equilibrium* scheme computes a local chemical equilibrium using the Gibbs energy minimization (see Drummond et al. 2018a). This scheme calculates mole fractions of a larger number of chemical species under a wider range of elemental abundances and thermodynamical conditions, but assumes chemical equilibrium. Our chemical *relaxation* scheme is similar to that of Cooper & Showman (2006). Our scheme relaxes CO and N_2 mole fractions to their equilibrium values at a time-scale of the rate-limiting step of CO–CH_4 conversion ($H + H_2CO + M \longrightarrow CH_3O + M$) and the net N_2–NH_3 conversion reaction ($N_2 + 3H_2 \rightleftharpoons 2NH_3$), respectively, and computes CH_4, H_2O, and NH_3 mole fractions from the mass balance assuming all C is contained in CO and CH_4, all O is in CO and H_2O, and all N is in N_2 and NH_3 (see Drummond et al. 2018b, c). The chemical *kinetics* scheme solves stiff ordinary differential equations describing chemical production and loss of chemical species in a chemical network of choice (see Drummond et al. 2020) using the DLSODES solver from the FORTRAN library ODEPACK (Hindmarsh 1983). For the chemical kinetics scheme, we use the Venot et al. (2019) chemical network with 30 neutral chemical species and 181 reversible reactions that had been reduced from the larger experimentally validated network of Venot et al. (2012) with the ANSYS© CHEMKIN-PRO REACTION WORKBENCH[1], with photodissociation reactions excluded from the reduction. All mentioned chemical networks are available via the KIDA data base[2] (Wakelam & KIDA Team 2012).

We neglect photochemistry and clouds in this work. Photochemistry generally becomes important at pressures near or less than the lowest included in our modelled domain (Baeyens et al. 2022), while the effects of clouds have been studied in several other works (Lee et al. 2016; Lines et al. 2018a, b, 2019; Christie et al. 2021, 2022; Roman et al. 2021). However, it is important to note that observations do suggest that some hot Jupiter atmospheres are cloud-free (Sing et al. 2016; Nikolov et al. 2018, 2022; Wakeford et al. 2018; Alam et al. 2021; Sheppard et al. 2021; Ahrer et al. 2022), so the assumption of a cloud-free atmosphere is a reasonable one for some planets.

2.2 Model setup and simulation parameters

We adopt the same basic model setup as Drummond et al. (2020). We use a horizontal resolution of 2.5° longitude by 2° latitude and 66 vertical levels equally spaced in height. Such a choice of grid resolution results in all our simulations being convectively stable, and thus not requiring a dry static adjustment. It is possible that the large-scale flow compensated for transport otherwise performed by unresolved convective or sub-grid scale motions, but this effect would have been minor and localized. We initialize the model at rest with a pressure-temperature profile from the 1D radiative-convective-chemistry model ATMO (e.g. Drummond et al. 2016). Such a profile, representing a dayside average, is calculated for each planet under the assumption of chemical equilibrium for species present in the Venot et al. (2012) chemical network, and used to derive a column-averaged specific gas constant and specific heat capacity as well as to adjust the vertical extent of the UM to cover a range of pressures from $\sim 2 \times 10^7$ Pa to ~ 1 Pa. Chemical species abundances in simulations using the chemical kinetics scheme are initialized

---

[1] ANSYS, Inc., San Diego, 2017, Chemkin-Pro 18.2.
[2] https://kida.astrochem-tools.org/

Table 1. Stellar parameters used for each simulation.

Parameter	Unit	HAT-P-11	HD 189733	HD 209458	WASP-17
Type		K4	K1-K2	G0	F4
Radius	m	4.75×10^8	5.23×10^8	8.08×10^8	11.01×10^8
Effective temperature	K	4800	5050	6100	6600
Stellar constant at 1 au	$W\,m^{-2}$	298.48	454.37	2335.45	5698.12
$\log_{10}$(surface gravity)	cgs	4.50	4.53	4.38	4.00
Metallicity	dex	0.300	-0.030	0.014	-0.500

Table 2. Planetary parameters used for each simulation. Parameters derived from the input stellar and planetary parameters or obtained after the model reached a pseudo-steady state are reported in the last two rows.

Parameter	Unit	HAT-P-11b	HD 189733b	HD 209458b	WASP-17b
Inner radius	m	2.72×10^7	8.05×10^7	9.00×10^7	13.51×10^7
Domain height	m	0.46×10^7	0.32×10^7	0.90×10^7	3.70×10^7
Semimajor axis	au	0.05259	0.03142	0.04747	0.05135
Orbital period	Earth day	4.888	2.219	3.525	3.735
Rotation rate	$rad\,s^{-1}$	1.49×10^{-5}	3.28×10^{-5}	2.06×10^{-5}	1.95×10^{-5}
Surface gravity[a]	$m\,s^{-2}$	13.20	21.50	9.30	3.31
Specific gas constant	$J\,K^{-1}\,kg^{-1}$	3514.3	3516.1	3516.6	3518.7
Specific heat capacity	$J\,K^{-1}\,kg^{-1}$	1.24×10^4	1.25×10^4	1.28×10^4	1.32×10^4
Stellar irradiance[b]	$W\,m^{-2}$	0.11×10^6	0.46×10^6	1.04×10^6	2.16×10^6
Effective temperature[c]	K	813	1162	1391	1622

Notes. [a]Assuming the bottom boundary is at 2×10^7 Pa.

[b]Calculated as $F_{1au}(1/a)^2$, where F_{1au} is the stellar constant at 1 au, and a is the semimajor axis.

[c]Calculated at pseudo-steady state as $(OLR/\sigma)^{1/4}$, where OLR is the global mean top-of-the-atmosphere outgoing longwave radiation, and σ is the Stefan–Boltzmann constant.

to their chemical equilibrium abundances derived for the pressure-temperature profile described above. Both models (ATMO and the UM) use the same, solar elemental abundances, namely a protosolar value for He, meteoritic values for Li and Cs, and photospheric values for Na and Rb from Asplund et al. (2009), and updates for C, N, O, and K from Caffau et al. (2011). The UM accounts for the heat flux from the planet interior by adding an upward flux corresponding to an intrinsic temperature of 100 K at the bottom boundary. The choice of having the same (rather than different) intrinsic temperature for all our targets relies on the theory of Tremblin et al. (2017), which suggests that the hot Jupiter radius inflation problem could be solved by a downward advection of potential temperature rather than a high internal flux, which implies that the choice of intrinsic temperature might be less critical than the simulation length. Since such advection occurs on a time-scale of thousands of years (Sainsbury-Martinez et al. 2019), we recognize that our simulations are too short for the deep atmosphere to fully evolve, and hence focus our further analysis on the upper atmosphere only. Additionally, we rely on the finding by Drummond et al. (2020, their Appendix C) that HD 209458b simulations with a cold and hot initial pressure-temperature profile showed that the deep atmosphere of this planet does not affect its upper atmosphere dynamics and chemistry, as the quench point for all six chemical species of interest (H_2O, CO, CO_2, CH_4, NH_3, HCN) lies above (towards lower pressures) the region of the atmosphere that has not reached a steady state by the end of the simulations.

The UM uses separate time-steps for the dynamics, radiative transfer, and chemistry, for which we adopt 30, 150, and 3750 s, respectively, as a balance between accuracy and computational efficiency. All simulations are integrated for a 1000 Earth days (i.e. 8.64×10^7 s) providing a pseudo-steady state for the upper atmosphere (diagnosed by analysing the evolution of the global maximum wind velocities, the global mean top-of-the-atmosphere

net energy flux, and the total mass of opacity sources, see Appendix B for details), while the deeper atmosphere is likely to still be evolving. During the model run time, we use low-resolution spectral files that have 32 spectral bands covering 0.2–322 μm and a maximum of 21 k-coefficients per band. For synthetic observations, we use high-resolution spectral files that have 500 spectral bands covering 2–10 000 μm (to better capture absorption features of chemical species of interest) and a maximum of 15 k-coefficients per band.

Stellar and planetary parameters used to simulate each of our targets with ATMO and the UM are obtained from the TEPCat data base[3] (Southworth 2011) and are summarized in Tables 1 and 2, respectively. For the stellar spectrum, we use the Kurucz spectra[4] for HD 189733 and HD 209458, and the PHOENIX BT-Settl spectra (Rajpurohit et al. 2013) for HAT-P-11 and WASP-17.

Following Drummond et al. (2020), we perform a pair of simulations per new target, HAT-P-11b and WASP-17b, with each simulation pair consisting of a simulation using the chemical equilibrium scheme and another using the chemical kinetics scheme. From now on we refer to these simulations as the 'equilibrium' and 'kinetics', respectively. These simulations required approximately 5.8 and 8.9 d of wall time per equilibrium and kinetics simulation, respectively, using 216 cores on the DiRAC DIaL supercomputing facility.

3 RESULTS

Here, we describe the dynamical, thermal, and chemical structure of the atmospheres of HAT-P-11b, HD 189733b, HD 209458b, and WASP-17b, simulated with the UM using the chemical equilibrium

[3]https://www.astro.keele.ac.uk/jkt/tepcat/
[4]http://kurucz.harvard.edu/stars.html
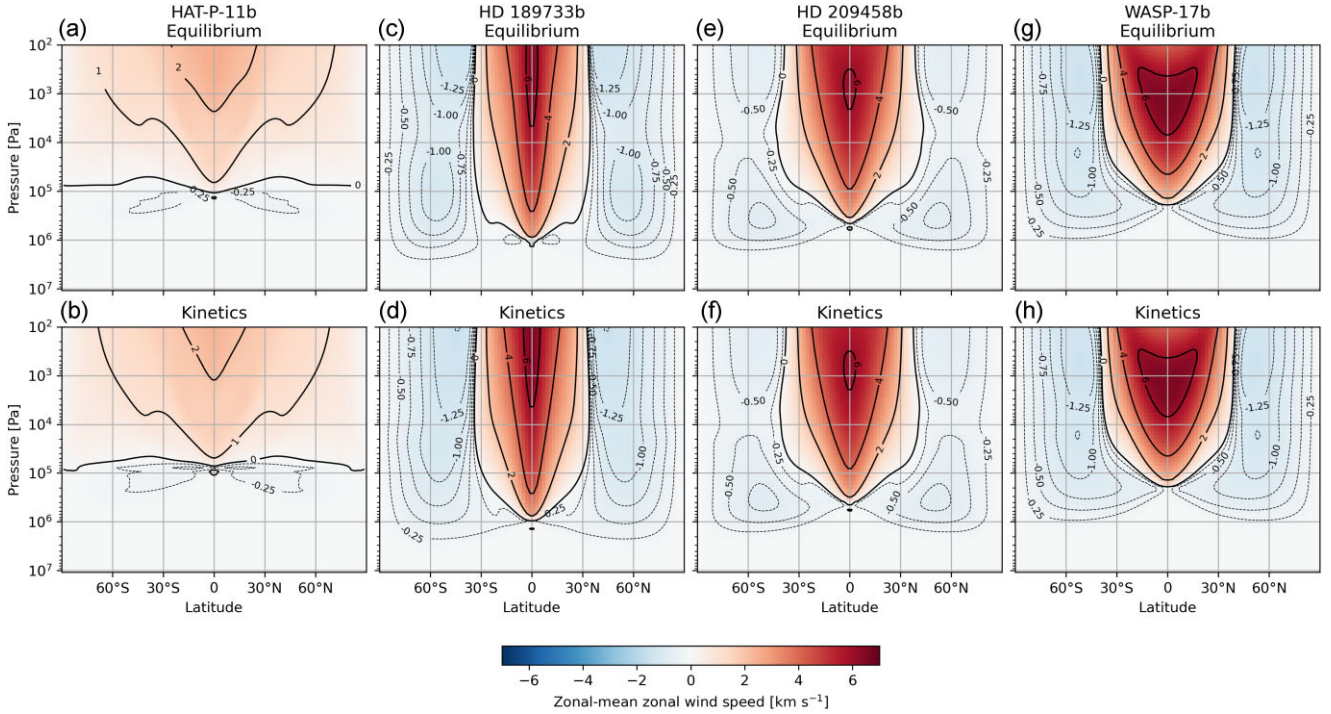
Figure 1. Zonal-mean zonal wind speed from HAT-P-11b, HD 189733b, HD 209458b, and WASP-17b equilibrium (top row) and kinetics (bottom row) simulations. For the eastward flow, the variability is additionally highlighted in black thick solid contours with $2\,\mathrm{km\,s^{-1}}$ intervals, and for the westward flow, it is highlighted in black thin dashed contours with $0.25\,\mathrm{km\,s^{-1}}$ intervals.

and chemical kinetics scheme. That description is followed by a discussion of the impact of the choice of a chemical scheme on the synthetic observations of these atmospheres.

3.1 Dynamical structure

Eastward (prograde) zonal flow dominates the atmospheric circulation of HAT-P-11b, HD 189733b, HD 209458b, and WASP-17b (Figs 1 and C1–C2). The speed and spatial extent of the eastward zonal flow vary from planet to planet, as do the characteristics of the weaker westward (retrograde) zonal flows located deeper than and/or poleward of the eastward flow. While the dynamical structure differs between planets, it is similar between their respective equilibrium and kinetics simulations.

For HAT-P-11b (Figs 1a and b), the eastward flow extends from pole to pole and down to $\sim 1 \times 10^5$ Pa, and has the maximum zonal-mean zonal wind speed at the equator of $2.6\,\mathrm{km\,s^{-1}}$ at 1.7×10^2 Pa in the equilibrium simulation, and $2.4\,\mathrm{km\,s^{-1}}$ at 1.0×10^2 Pa in the kinetics simulation. The westward flow prevails at deeper pressures, and a pair of westward zonal jets forms between 1×10^5 and 3×10^5 Pa, having the zonal-mean zonal wind speed maxima at $\pm 10°$ latitude of $0.33\,\mathrm{km\,s^{-1}}$ in the equilibrium simulation, and $0.62\,\mathrm{km\,s^{-1}}$ in the kinetics simulation. Showman, Lewis & Fortney (2015) predicted a similar atmospheric circulation for a moderately irradiated, slowly rotating hot Jupiter in their 'W$\Omega_{\rm slow}$'[5] cloud-free simulation with the SPARC/MITGCM 3D hydrodynamics-radiation model (their figs 3 and 4) to that we find for HAT-P-11b. However, their 'W$\Omega_{\rm slow}$' case is

the closest but not equivalent to our HAT-P-11b simulations in terms of the stellar and planetary parameters used.

For HD 189733b (Figs 1c and d), our model predicts an emergence of the eastward equatorial zonal jet, which is more prominent than that of HAT-P-11b. The HD 189733b equatorial zonal jet spans $\pm 30°$ latitude and extends down to $\sim 1 \times 10^6$ Pa, having the maximum zonal-mean zonal wind speed at the equator of $6.4\,\mathrm{km\,s^{-1}}$ at 3.5×10^2 Pa in the equilibrium simulation, and $6.5\,\mathrm{km\,s^{-1}}$ at 2.9×10^2 Pa in the kinetics simulation. The westward flow controls the circulation elsewhere. Two pair and one pair of westward zonal jets emerge in the equilibrium and kinetics simulations, respectively, but the zonal-mean zonal wind speed maxima between all these westward zonal jets are the same in both simulations, and are equal to $1.5\,\mathrm{km\,s^{-1}}$, and are located at $\pm 40°$ latitude at $\sim 1 \times 10^2$ Pa.

For HD 209458b (Figs 1e and f), the emergent eastward equatorial zonal jet is similar to that of HD 189733b, except for being wider, especially between 1×10^3 and 1×10^5 Pa, and shallower. The HD 209458b equatorial zonal jet spans $\pm 40°$ latitude and extends down to $\sim 5 \times 10^5$ Pa, having the maximum zonal-mean zonal wind speed at the equator of $6.1\,\mathrm{km\,s^{-1}}$ at 8.7×10^2 Pa in both simulations. The westward flow occurs elsewhere. Two pairs of westward zonal jets emerge in both simulations, with the jet pair located at $\pm 50°$ latitude at $\sim 5 \times 10^5$ Pa having faster zonal-mean zonal wind speeds, with maxima of $0.8\,\mathrm{km\,s^{-1}}$, than the jet pair located at lower pressures.

For WASP-17b (Figs 1g and h), our simulations show an eastward equatorial zonal jet similar to those of HD 189733b and HD 209458b, except for it being even shallower. The WASP-17b equatorial zonal jet spans $\pm 40°$ latitude and extends down to 2×10^5 Pa, having the maximum zonal-mean zonal wind speed at the equator of $6.6\,\mathrm{km\,s^{-1}}$ at 1.5×10^3 Pa in both simulations (which is comparable with $5\,\mathrm{km\,s^{-1}}$ at $\sim 1 \times 10^4$ Pa estimate from Kataria et al. 2016). The

---

[5]HD 189733b as $R_{\rm planet} = 1.15 \times R_{\rm Jupiter} = 8.04 \times 10^7$ m, $g = 21.4\,\mathrm{m\,s^{-2}}$, $R_{\rm s} = 3714.3\,\mathrm{J\,K^{-1}\,kg^{-1}}$, $c_{\rm p} = 1.30 \times 10^4\,\mathrm{J\,K^{-1}\,kg^{-1}}$, metallicity $= 1 \times$ solar, but with the following parameters modified: $a = 0.0789$ au, $F_{\rm star} = 7.37 \times 10^4\,\mathrm{W\,s^{-2}}$, $T_{\rm orb} = 8.8$ Earth days, $\Omega = 8.264 \times 10^{-6}\,\mathrm{rad\,s^{-1}}$.
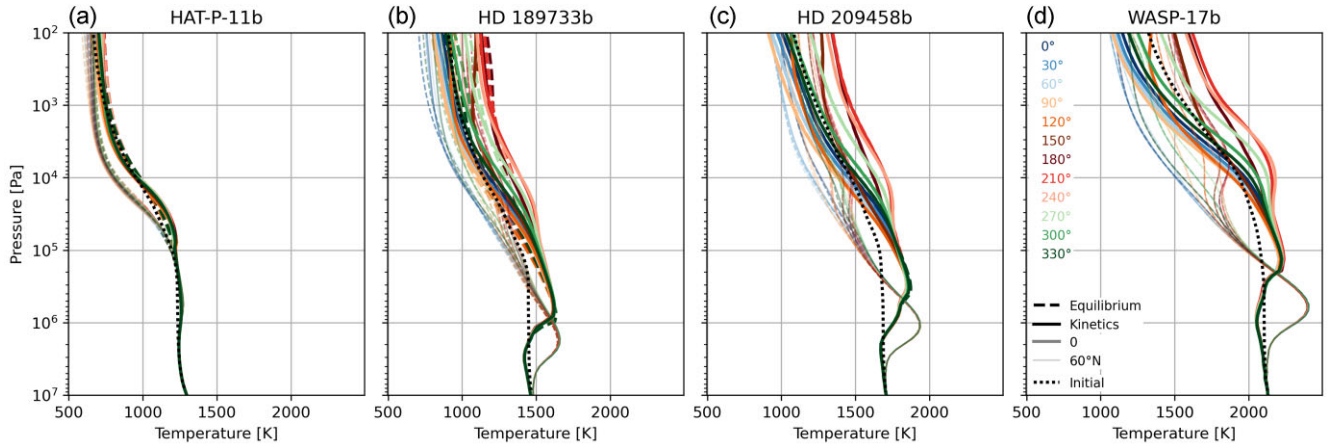
Figure 2. Pressure-temperature profiles for different longitudes around the equator (thick lines in bright colours) and 60°N (thin lines in faded colours) from HAT-P-11b, HD 189733b, HD 209458b, and WASP-17b equilibrium (dashed) and kinetics (solid) simulations. Pressure-temperature profiles used to initialize each pair of 3D simulations are the dayside average profiles from the respective 1D ATMO equilibrium simulations (dotted).

westward flow supports two pairs of zonal jets located at ±50° latitude in both simulations. The jet pair at $\sim 1 \times 10^3$ Pa has faster zonal-mean zonal wind speeds, with maxima of $1.5\,\mathrm{km\,s^{-1}}$, than the jet pair located at higher pressures.

3.2 Thermal structure

The thermal structure of the atmospheres of HAT-P-11b, HD 189733b, HD 209458b, and WASP-17b differs between planets but is similar between their respective equilibrium and kinetics simulations. To explore the atmospheric thermal structure of these planets, we analyse their pressure-temperature vertical profiles (Fig. 2).

The simulated HAT-P-11b atmosphere is the coldest and the most thermally uniform relative to atmospheres of the other three planets in our sample (Fig. 2a). HAT-P-11b receives the lowest stellar irradiance, as it orbits the coldest host star at the largest orbital radius in our sample, resulting in the smallest zonal and meridional temperature gradients in the planet's atmosphere. The HAT-P-11b equilibrium and kinetics simulations predict slightly different thermal structures, especially closer to the equator. At the equator between 1×10^2 and 1×10^4 Pa, temperatures are lower by up to 10 K in the kinetics simulation relative to the equilibrium one, while between 1×10^4 and 1×10^5 Pa temperatures are higher by up to 10 K in the kinetics simulation relative to the equilibrium one.

The simulated HD 189733b atmosphere (Fig. 2b) is hotter than that of HAT-P-11b. HD 189733b receives a larger stellar irradiance, as it orbits a hotter host star at a smaller orbital radius (in fact, the smallest). This leads to larger zonal and meridional temperature gradients in the planet's atmosphere. The HD 189733b equilibrium and kinetics simulations also predict different thermal structures, but the temperature differences are within 5–10 per cent (Drummond et al. 2020).

The simulated HD 209458b atmosphere (Fig. 2c) is even hotter than that of HD 189733b. HD 209458b receives a larger stellar irradiance, as it orbits a hotter host star but at a larger orbital radius. This results in its zonal and meridional temperature gradients being similar to those of HD 189733b. The HD 209458b equilibrium and kinetics simulations predict similar thermal structures, with the temperature differences being <1 per cent (Drummond et al. 2020).

The simulated WASP-17b atmosphere (Fig. 2d) is the hottest, and has the largest zonal and meridional temperature gradients. In fact, its atmosphere is so hot that its equilibrium and kinetics simulations

predict almost identical thermal structures due to extremely short chemical time-scales.

3.3 Chemical structure

The abundances of chemical species in our equilibrium simulations trace the pressure-temperature structure of the atmosphere, as is expected from the Gibbs energy minimization. In our kinetics simulations, however, they depart from equilibrium due to transport-induced quenching, which is a homogenization of chemical abundance gradients by atmospheric advection (Moses 2014). Because transport-induced quenching depends on the difference between the time-scale of chemical reactions and the time-scale of advection, such quenching occurs at different pressure levels, or depths, in the atmosphere for different chemical species (Visscher & Moses 2011; Agúndez et al. 2014). CH_4 and CO quenching depends on the time-scale of CH_4–CO interconversion and the competition between CO and H_2O for being the main carrier of atomic oxygen O, causing CH_4, CO, and H_2O to quench at a similar depth. CO_2 quenching, however, depends on the combined time-scale of CO–CO_2 conversion and H_2O destruction, with the latter being the main OH source for $CO+OH \rightarrow CO_2 + H$. CO_2 maintains pseudo-equilibrium with CO and H_2O while atmospheric conditions sustain efficient CO–CO_2 conversion, but it quenches when it is no longer the case (Tsai et al. 2018). NH_3 and HCN quenching is the least understood, but it generally depends on the time-scale of N_2–NH_3 interconversion and CH_4–CO interconversion, with the latter impacting the availability of C for a C–N bond. Because coupled NH_3 and CH_4 chemistry needs to produce HCN first (Moses et al. 2011), NH_3 quenches before HCN does. Transport-induced quenching also varies in strength, which in our simulations could be thought of as a departure of the disequilibrium abundance not caused by photochemistry (as photochemistry is less relevant at pressures where transport-induced quenching occurs) from equilibrium that depends on the wind speed and direction. When all three types of transport-induced quenching occur in an atmosphere, zonal quenching would likely occur first due to zonal winds being the fastest on average, with meridional and vertical quenching being second and third, respectively. Therefore, capturing the 3D nature of atmospheric flows is important to correctly resolve transport-induced quenching.

While the dynamical and thermal structures of the atmospheres of HAT-P-11b, HD 189733b, HD 209458b, and WASP-17b are

broadly similar between their respective equilibrium and kinetics simulations, their chemical structure is markedly different. To explore the difference in the atmospheric chemical structure between equilibrium and kinetics simulations, we analyse vertical profiles (Fig. 3, and Fig. C3 with different X-axes) and longitude–latitude cross-sections of chemical species mole fractions (Fig. 4). For the longitude–latitude cross-sections, we sampled our model data at a pressure level of the photosphere (i.e. where the value of the normalized contribution function is equal to 1, see Appendix C) in spectral bands[6] closest to the centre of the *Spitzer*/IRAC channels 3.6, 4.5, 5.8, and 8.0 µm that coincide with the peaks in the absorption cross-section of CH_4, CO, H_2O, and CH_4, respectively, and a band closest to 10.5 µm coinciding with the peak in NH_3 absorption cross-section. We selected a single spectral band for each *Spitzer*/IRAC channel instead of a range of bands as did Drummond et al. (2018c) to simplify the cases of 'convoluted' photospheres (Dobbs-Dixon & Cowan 2017), for which the contribution function has multiple peaks when a range of absorption coefficients from several spectral bands contributes to the total absorption.

3.3.1 HAT-P-11b

For HAT-P-11b, transport-induced quenching occurs at the boundary between the superrotating and the retrograde flow (Figs 1b and 3a–f). At high latitudes (e.g. 60°N), it occurs fully within the retrograde flow, while closer to the equator, it occurs in a calmer but more variable wind regime, which causes the variability in the chemical species mole fractions between 1×10^5 and 1×10^6 Pa.

CH$_4$, CO, and H$_2$O quench zonally and vertically, with the depth and strength of either direction of quenching varying with latitude (Figs 3a, b, d). At the equator, CH$_4$, CO, and H$_2$O quench at $\sim 1 \times 10^6$ Pa, where their vertical profiles from the kinetics simulation depart from those at equilibrium. Between 1×10^3 and 1×10^5 Pa, zonal quenching dominates over vertical, as the profiles show almost no change zonally (with longitude) but still change vertically (with decreasing pressure). Between 1×10^2 and 1×10^3 Pa, however, both directions of quenching become equally strong, causing the profiles to stay constant with decreasing pressure until the top of our model domain. At 60°N, CH$_4$, CO, and H$_2$O quench at the same depth as at the equator, but both quenching directions become equal in strength towards higher pressures, at 2×10^5 Pa, than at the equator. Due to these differences in quenching depth and strength with latitude, CH$_4$, CO, and H$_2$O mole fractions reach nearly the same value at 1×10^3 Pa, and form a relatively uniform layer with longitude and latitude between 1×10^2 and 1×10^3 Pa. This contrasts our equilibrium simulation, where they retain zonal and meridional gradients in this layer. The homogenization of CH$_4$, CO, and H$_2$O abundances by atmospheric advection alters their spatial distribution at the pressure level of the photosphere (Fig. 4 first column). CH$_4$ mole fractions at the 3.6 and 8.0 µm photospheres decrease by up to a factor of 2 in the kinetics simulation relative to equilibrium one, but stay at $\sim 3 \times 10^{-4}$ in both simulations. H$_2$O mole fractions at the 5.8 µm photosphere change similarly to CH$_4$, and stay at $\sim 7 \times 10^{-4}$ in both simulations.

---

[6]Spectral band centre (in µm) and bounds (in µm):

   (i) 3.6 µm (3.5971223–3.6101083),

   (ii) 4.5 µm (4.484305–4.5045044),

   (iii) 5.8 µm (5.780347–5.8139535),

   (iv) 8.0 µm (8.0–8.064516),

   (v) 10.5 µm (10.416667–10.526316).

CO mole fractions at the 4.5 µm photosphere, however, increase from $\sim 1 \times 10^{-6}$ to $\sim 1 \times 10^{-4}$ poleward of $\pm 40°$ latitude, and smooth out the meridional gradient, causing CO mole fractions to stay at $\sim 2 \times 10^{-4}$ at the 4.5 µm photosphere in the kinetics simulation.

CO$_2$ maintains a pseudo-equilibrium with CO and H$_2$O between 1.5×10^4 and 3×10^5 Pa, and quenches zonally and vertically between 1×10^2 and 1.5×10^4 Pa at a value of $\sim 1 \times 10^{-7}$ (Fig. 3c). This differs from our equilibrium simulation, where CO$_2$ varies with longitude and latitude between 1×10^2 and 1×10^4 Pa, and maintains zonal and meridional gradients of up two orders of magnitude.

NH$_3$ and HCN quench in a similar manner to CH$_4$ and CO, but unlike CH$_4$ and CO, their mole fractions mostly increase due to quenching (Figs 3e and f). As a result, NH$_3$ mole fractions at the 10.5 µm photosphere increase in a way with that produces a nearly uniform longitude and latitude NH$_3$ distribution, with NH$_3$ mole fractions staying at $\sim 2 \times 10^{-6}$, because the meridional gradient between $\sim 4 \times 10^{-6}$ at the poles and $\sim 4 \times 10^{-7}$ at the equator present at equilibrium is eliminated.

Results from our HAT-P-11b equilibrium and kinetics simulations for CH$_4$, CO, H$_2$O, CO$_2$, and NH$_3$ vertical profiles at the equator agree with those of Moses et al. (2021) from their pseudo-2D chemical equilibrium and kinetics simulations of an exo-Neptune[7] with 700 K effective temperature rotating at 0.067294 au from a K5V star[8] (their fig. 6). This agreement supports the prediction made by both their and our study that H$_2$O>CH$_4$>CO in terms of abundance between 1×10^2 and 1×10^7 Pa in atmospheres of such planets. However, our equatorial HCN vertical profiles from the kinetics simulation show mole fractions of $\sim 1 \times 10^{-9}$, which is 2–3 orders of magnitude lower than those presented in their study. This is likely caused by the difference in HCN treatment between Venot et al. (2019) and Moses et al. (2013) chemical networks.

3.3.2 HD 189733b and HD 209458b

Vertical profiles of CH$_4$, CO, H$_2$O, CO$_2$, NH$_3$, and HCN were discussed in Drummond et al. (2020). Here, we briefly repeat their major conclusions, and discuss the spatial distribution of CH$_4$, CO, H$_2$O, and NH$_3$ at the pressure level of the photosphere.

For our simulations of HD 189733b and HD 209458b, transport-induced quenching occurs at the base of the superrotating jet, or at higher pressures and within the retrograde flow (Figs 1d, f, 3g–r).

For HD 189733b, CH$_4$, CO, H$_2$O, and NH$_3$ quench zonally, meridionally, and vertically, with the evidence for meridional quenching discussed in Drummond et al. (2018b). As a result, CH$_4$ mole fractions at the 3.6 and 8.0 µm photospheres are homogenized by atmospheric advection in a way that reduces their zonal and meridional gradients, leaving only a small, $\sim 3 \times 10^{-5}$ to $\sim 4 \times 10^{-5}$ equator-to-pole gradient in the kinetics simulation (Fig. 4 second column). CO and H$_2$O mole fractions at the 5.8 and 4.5 µm photospheres, respectively, change mostly on the nightside poleward of $\pm 30°$ latitude, but with an opposite sign: H$_2$O mole fractions decrease by about a factor of 2 and stay at $\sim 4.7 \times 10^{-4}$, while CO mole fractions increase by about a factor of 2 and stay at $\sim 4.9 \times 10^{-4}$. Therefore, CO>H$_2$O>CH$_4$ in terms of abundance in the upper atmosphere of HD 189733b. NH$_3$ mole fractions at the 10.5 µm photosphere change similarly to CH$_4$, and stay at $\sim 3 \times 10^{-6}$ in the kinetics simulation.

---

[7]$R_{planet} = 0.4 \times R_{Jupiter} = 2.80 \times 10^7$ m, $T_{orb} =$ 8.48 Earth days, $\Omega = 8.57 \times 10^{-6}$ rad s^{-1}, g = 10 m s^{-2}, metallicity = 1 × solar

[8]$R_{star} = 0.7 \times R_{Sun} = 4.87 \times 10^8$ m, T_{eff} = 4500 K, $\log_{10}(g)$ = 4.50(cgs)
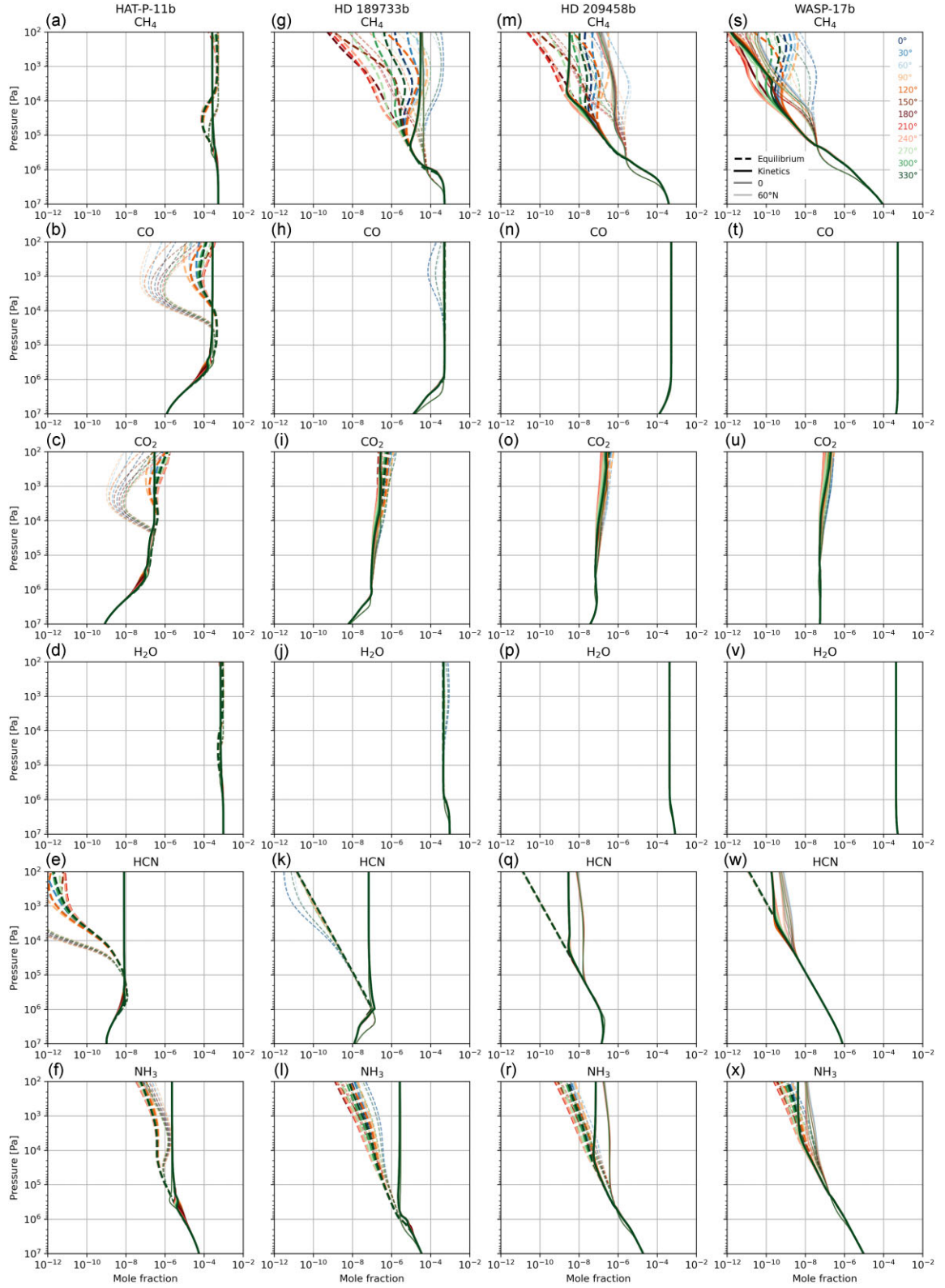
Figure 3. Vertical profiles of chemical species mole fractions for different longitude points around the equator and 60°N, from the equilibrium (dashed) and kinetics (solid) simulations of HAT-P-11b (first column), HD 189733b (second column), HD 209458b (third column), and WASP-17b (fourth column).

For HD 209458b, CH$_4$, CO, H$_2$O, and NH$_3$ quench zonally and vertically. As a result, CH$_4$ mole fractions at the 3.6 and 8.0 μm photospheres are homogenized by atmospheric advection in

a way that reduces their zonal gradient, but leaves an equator-to-pole gradient of $\sim 1 \times 10^{-9}$ to $\sim 1 \times 10^{-6}$ in the kinetics simulation (Fig. 4 third column), which is larger than that found
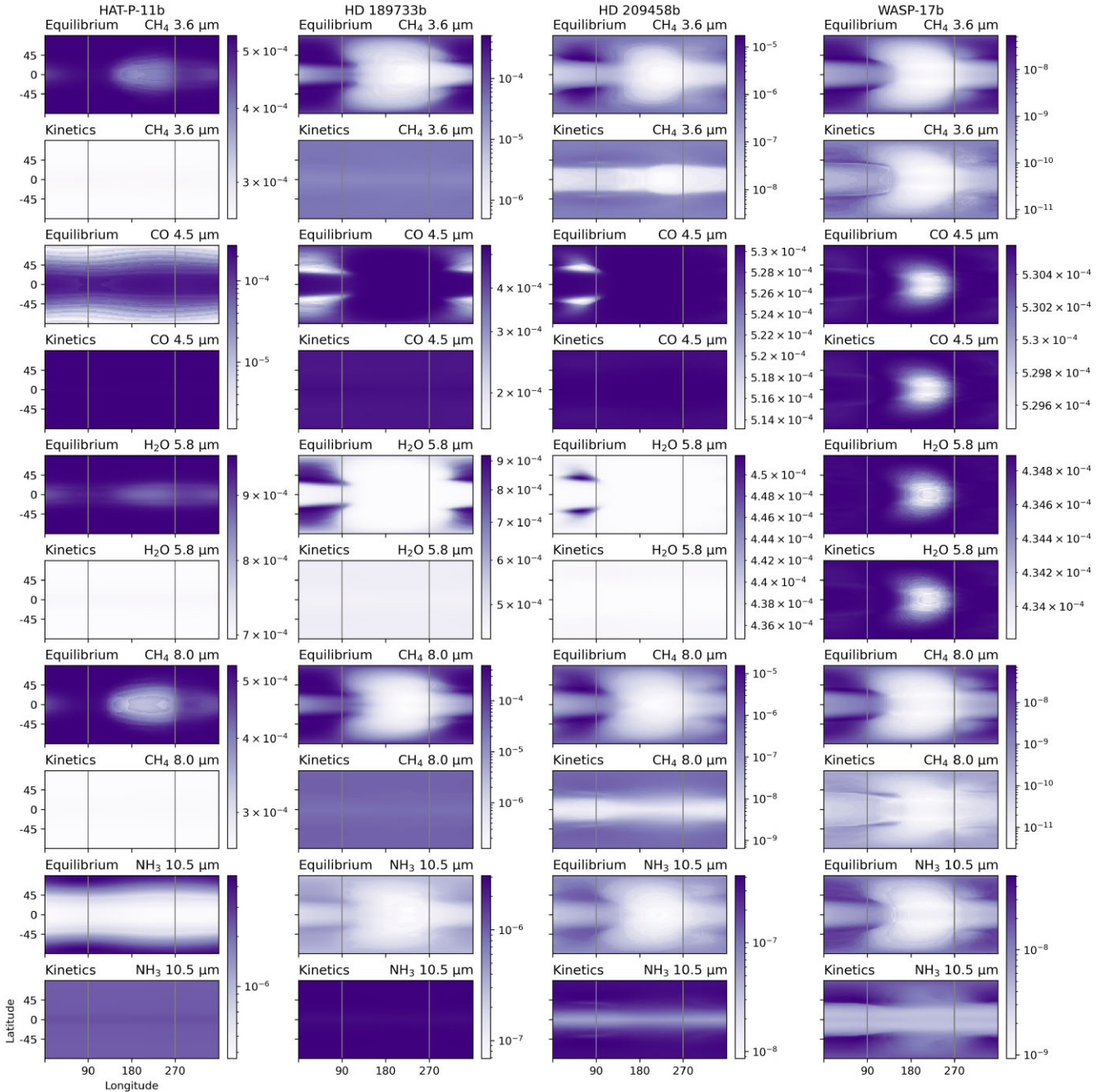
Figure 4. Chemical species mole fractions at a pressure level of the photosphere in individual spectral bands closest to 3.6, 4.5, 5.8, 8.0, and 10.5 μm associated with the peaks in absorption from CH$_4$, CO, H$_2$O, CH$_4$, and NH$_3$, respectively, from the equilibrium and kinetics simulations of HAT-P-11b (first column), HD 189733b (second column), HD 209458b (third column), and WASP-17b (fourth column). The substellar point is located at 180° latitude. Grey grid lines show 90° and 270° longitude.

for HD 189733b. CO and H$_2$O mole fractions at the 5.8 and 4.5 μm photospheres, respectively, change less than those for HD 189733b and only between 0 and 100°E poleward of ±40° latitude, but still with an opposite sign: H$_2$O mole fractions decrease and stay at ~4.4 × 10^{-4}, while CO mole fractions increase and stay at ~5.3 × 10^{-4}. Therefore, CO>H$_2$O>CH$_4$ in terms of abundance in the upper atmosphere of HD 209458b. NH$_3$ mole fractions at the 10.5 μm photosphere change similarly to CH$_4$, resulting in a small, ~5 × 10^{-8} to ~4 × 10^{-7} equator-to-pole gradient in the kinetics simulation.

3.3.3 WASP-17b

For WASP-17b, transport-induced quenching occurs at lower pressures than that for the other three planets. At latitudes occupied by the superrotating jet, it occurs near the fastest part of the jet, while elsewhere it occurs deeper and within the retrograde flow (Figs 1h and 3s–x).

As WASP-17b's atmosphere is warmer than those of the other three planets, CO is thermodynamically favoured over CH$_4$ in such a way that makes CO more abundant than CH$_4$ throughout our entire model domain. With H$_2$O adjusting accordingly, CO>H$_2$O>CH$_4$ in

terms of abundance, which is similar to the upper atmospheres of HD 189733b and HD 209458b. Preferential production of CO and H_2O over CH_4 causes CO and H_2O spatial variability to be smaller than that of CH_4, which is why below we discuss CH_4 vertical profiles only.

CH_4 quenches zonally and vertically, with zonal quenching dominating over vertical, and quenching depth varying with longitude and latitude (Fig. 3s). On the dayside at the equator, CH_4 quenches at 5×10^2 Pa, while on the nightside at the equator it quenches deeper, with the quenching pressure level increasing from 1×10^3 Pa at 270°E to 7×10^3 Pa at 90°E. Therefore, at the equator, CH_4 quenching occurs at different pressure levels for all longitudes. However, at high latitudes, it occurs at a single and higher pressure than that at the equator, which is the same for all longitudes (e.g. at 1×10^5 Pa at 60°N). This leads to an overall tendency of CH_4 vertical profiles to evolve towards the dayside equilibrium values, which causes CH_4 mole fractions at the 3.6 and 8.0 μm photospheres to decrease in a way that retains their meridional gradient but reduces the zonal gradient (Fig. 4 fourth column). In the kinetics simulation, CH_4 mole fractions stay at $\sim 1 \times 10^{-11}$ on the dayside and at $\sim 1 \times 10^{10}$ to 1×10^{-9} on the nightside. CO mole fractions at the 4.5 μm photosphere stay at $\sim 5 \times 10^{-4}$, while H_2O mole fractions at the 5.8 μm photosphere stay at $\sim 4 \times 10^{-4}$ in both simulations.

CO_2 is at equilibrium throughout most of our model domain in the kinetics simulation, except for $<5 \times 10^2$ Pa between 330°E and 90°E on the nightside, where it is likely at pseudo-equilibrium with CO and H_2O (Fig. 3u). As a result, CO_2 mole fractions vary with longitude and latitude from $\sim 6 \times 10^{-8}$ at the substellar point to $\sim 1 \times 10^{-7}$ elsewhere, and the difference between equilibrium and kinetics simulations is small.

NH_3 and HCN quench zonally and vertically, with the depth and strength of either direction of quenching varying with longitude and latitude (Figs 3w and x). At the equator, NH_3 quenches at 3×10^4 Pa, with zonal quenching dominating over vertical between 3×10^3 and 3×10^4 Pa, and both directions of quenching becoming equal at lower pressures. At 60°N, NH_3 quenches deeper, at 7×10^4 Pa, with zonal quenching also dominating over vertical, especially on the nightside, up to the top of our model domain. Zonal quenching is weaker at 60°N than at the equator, which causes the 60°N profiles for different longitudes to diverge. As a result, NH_3 mole fractions at the 10.5 μm photosphere increase, and they increase by a higher amount poleward of ±40° latitude than elsewhere. This creates a more prominent, $\sim 4 \times 10^{-9}$ to $\sim 1 \times 10^{-8}$ equator-to-pole gradient in the kinetics simulation than at equilibrium. HCN spatial variability is similar to that of NH_3, but HCN quenches at lower pressures than NH_3, at 5×10^3 Pa at a mole fraction of $\sim 2 \times 10^{-10}$ and at 3×10^4 Pa at a mole fraction of $\sim 7 \times 10^{-10}$ at the equator and 60°N, respectively.

Results from our WASP-17b equilibrium simulation for CH_4, CO, H_2O, and NH_3 vertical profiles agree with those of Kataria et al. (2016) from their interpolation of 1D pressure-temperature profiles, averaged over the dayside, nightside, east and west terminator, obtained from WASP-17b[9] cloud-free simulation of the SPARC/MITGCM 3D hydrodynamics-radiation model on to a chemical equilibrium abundance pressure-temperature grid (their figs 6 and 7; note that instead of mole fractions they show mass mixing ratios, and one needs to multiply the former by about 10 for these species to convert

the former to the latter[10]). Such agreement is somewhat surprising, because it happens despite the difference in the jet structure predicted by the UM (one equatorial superrotating jet and two mid-latitude counterrotating jets, Fig. 1g) and the SPARC/MITGCM (one pole-to-pole superrotating jet, their fig. 2). This suggests that WASP-17b's thermal structure is mostly controlled by the stellar forcing rather than the atmospheric advection, making this planet a good target for the 1D and 2D modelling studies.

3.4 Synthetic observations

Here, we discuss the impact of the choice between the chemical equilibrium and chemical kinetics scheme on the synthetic observations derived from our simulations of the atmospheres of HAT-P-11b, HD 189733b, HD 209458b, and WASP-17b.
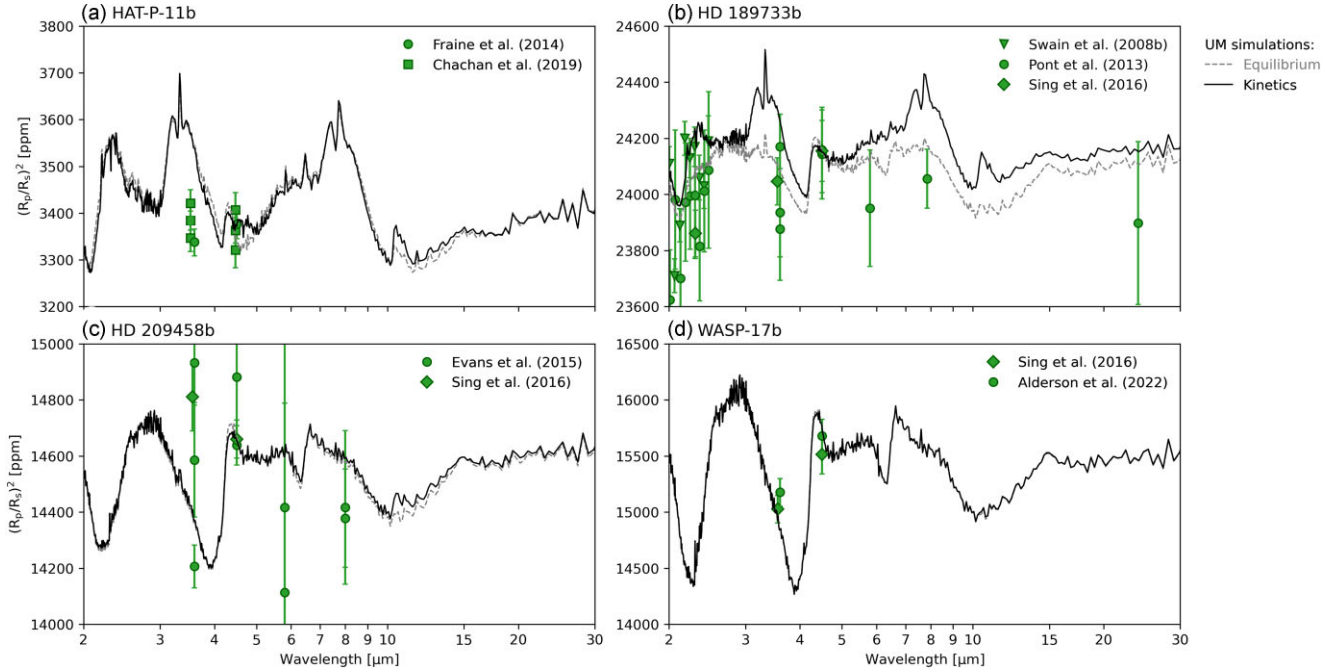
3.4.1 Transmission spectrum

Using the methodology of Lines et al. (2018a) updated recently by Christie et al. (2021), we calculate synthetic transmission spectra (Fig. 5, with differences shown in Fig. C7) and the contributions of major opacity sources to these spectra (Fig. 6) over the 2–30 μm range using the output from our equilibrium and kinetics simulations of the atmospheres of HAT-P-11b, HD 189733b, HD 209458b, and WASP-17b. The observed primary eclipse depth data were taken from the latest publications and observational data reviews, where possible, i.e. for HAT-P-11b, from Fraine et al. (2014, extended data table 1), and Chachan et al. (2019, table 2); for HD 189733b, from Swain, Vasisht & Tinetti (2008a, supplementary table 1), Pont et al. (2013, table 5), and Sing et al. (2016, fig. 1); for HD 209458b, from Evans et al. (2015, table 4), and Sing et al. (2016, fig. 1); and for WASP-17b, from Sing et al. (2016, fig. 1), and Alderson et al. (2022, table 3). Given 1.2–3.3 per cent uncertainty in the stellar and planetary radii (Southworth 2011) used as input into our model, we shifted our synthetic transmission spectra uniformly by a fixed value before comparing them to the observed transit depth data. The value of the shift was chosen so that the latest existing observations at 4.5 μm aligned with our model predictions.

Synthetic HAT-P-11b transmission spectra (Figs 5a and 6a) from our equilibrium and kinetics simulations differ at several wavelengths. The magnitude and cause of these differences varies, with the largest differences caused by the transport-induced quenching of CO and NH_3 (Section 3.3.1). In the region probed in transmission in the kinetics simulation, CO and NH_3 abundances increase by 2–3 orders of magnitude over those predicted at equilibrium. That causes CO and NH_3 to replace H_2O as the main contributor to the total transmission spectrum at 4.4–5.0 μm and 10.2–11.4 μm, respectively, and increase the transit depth by up to 60 and 45 ppm, respectively (including smaller contributions from other gases), in the kinetics simulation relative to the equilibrium one. Other, smaller (±20–30 ppm) differences between our transmission spectra are associated with the transport-induced quenching of CH_4, CO_2, H_2O, NH_3, and HCN. These differences are not dominated by the change in abundance of one gas, but are instead caused by the change in abundance of all of these gases. However, because abundances of

---

[9]$R_{planet} = 1.89 \times R_{Jupiter} = 13.21 \times 10^7$ m, $T_{orb} = 3.73$ Earth days, $\Omega = 1.95 \times 10^{-5}$ rad s^{-1}, g = 3.57 m s^{-2}, metallicity = $1 \times$ solar, $F_{star} = 2.14 \times 10^6$ W s^{-2}, $T_{eq} = 1738$ K

[10]The conversion factor from mole fraction to mass fraction is the ratio of the species molar mass to the mean molar mass of the background gas. The latter is about 2.33 g mol^{-1} for hot Jupiters. Therefore, the conversion factors are: CH_4 6.89, CO 12.02, H_2O 7.73, and NH_3 7.31.

Figure 5. Transmission spectra from the equilibrium (grey dashed) and kinetics (black solid) simulations of HAT-P-11b (a), HD 189733b (b), HD 209458b (c), and WASP-17b (d). UM transmission spectra were uniformly shifted by −760, −980, 140, −7200 ppm, respectively. The observed transit depths and their uncertainties are shown in green.
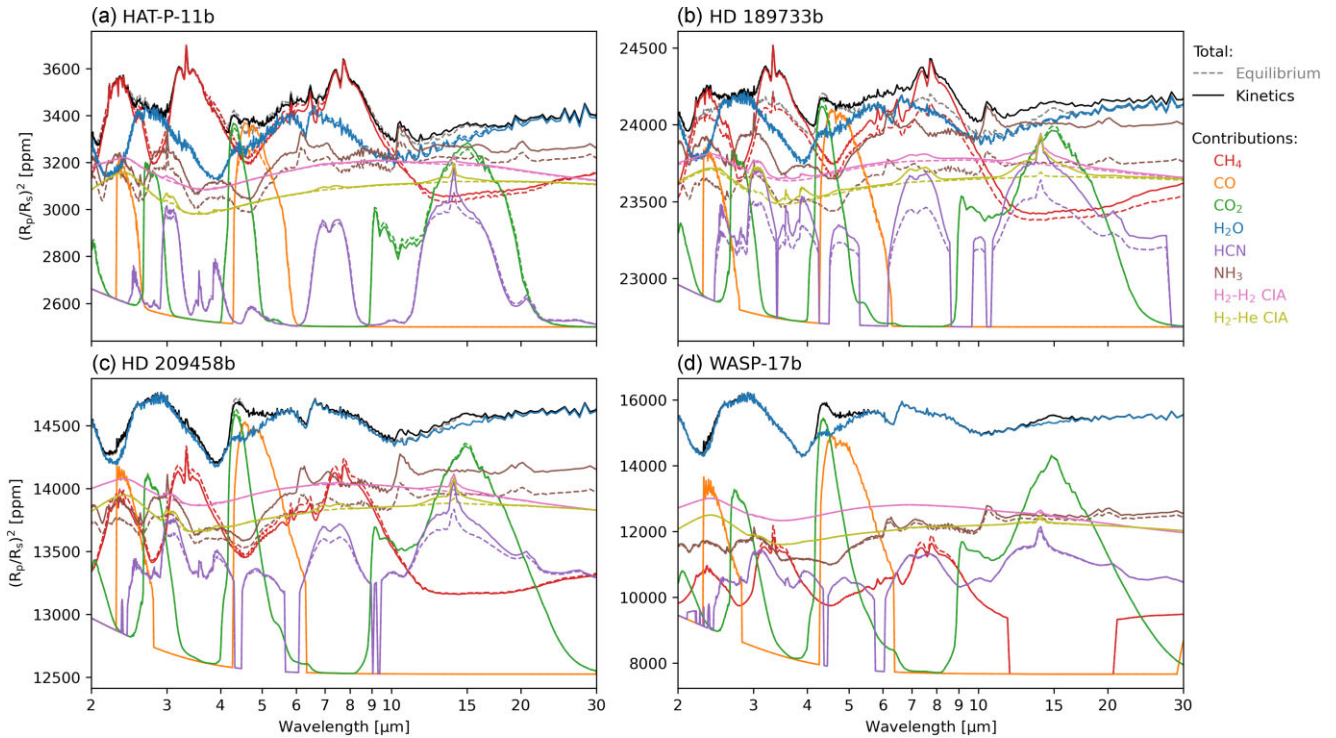
Figure 6. As in Fig. 5 but with the contributions from CH_4, CO, CO_2, H_2O, HCN, NH_3 absorption, and H_2–H_2 and H_2–He collision-induced absorption.

these gases often change in opposing directions, the corresponding differences between our spectra are small.

When compared to existing observations, our synthetic HAT-P-11b transmission spectra disagree with observations by Fraine et al. (2014) and Chachan et al. (2019). However, this disagreement supports the suggestion of Line & Parmentier (2016) and

Chachan et al. (2019) that the HAT-P-11b transmission spectrum could be explained by a relatively low atmospheric metallicity and uneven cloud cover. A further comparison with existing observations is required, especially with those shortward of 2 μm, but such a comparison is outside the scope of this study.

Synthetic HD 189733b transmission spectra (Figs 5b and 6b) from our equilibrium and kinetics simulations depart from each other throughout the entire wavelengths range considered in this work. The main cause of departure is the transport-induced quenching of CH_4, NH_3, and CO_2 (Drummond et al. 2020, and Section 3.3.2 in this work). In the region probed in transmission in the kinetics simulation, CH_4 abundance increases by 2–4 orders of magnitude at the eastern terminator, and stays similar to that predicted at equilibrium at the western terminator. This, together with a planet-wide, 2–3 orders of magnitude increase in NH_3 abundance, increases the transit depth by up to 150 ppm at 2.1–2.5 μm, 300 ppm at 3.0–4.1 μm, and 230 ppm at 7.0–9.5 μm (including smaller contributions from other gases) in the kinetics simulation relative to the equilibrium one. Despite the aforementioned increases in CH_4 and NH_3, the kinetics simulation predicts a smaller (by 30 ppm) transit depth at 4.2–4.5 μm than the equilibrium simulation. This is caused by an order of magnitude decrease in CO_2 abundance at the western terminator in the kinetics simulation relative to the equilibrium one. Lastly, and similarly to HAT-P-11b, NH_3 abundance increases in HD 189733b kinetics simulation so that NH_3 replaces H_2O as the main contributor to the total transmission spectrum at 10.0–11.6 μm, and causes an increase the transit depth by up to 200 ppm (including smaller contributions from H_2O, CH_4, and HCN) at these wavelengths.

When compared to existing observations, our synthetic HD 189733b transmission spectrum from the kinetics simulation partly agrees with observations of Swain et al. (2008a; reliability of which had been questioned in Sing et al. 2009), but predicts larger transit depths than those presented in Pont et al. (2013) and Sing et al. (2016). In fact, in the case of the latter two studies the spectrum from our kinetics simulation overestimates the observed transit depths more severely than the spectrum from our equilibrium simulation. This suggests that if the atmosphere of HD 189733b is cloud- and haze-free, it is closer to being at chemical equilibrium. However, without an observational constraint on the position of the spectrum continuum at the wavelengths range considered in this work, we cannot rule out a possibility that HD 189733b's transmission spectrum could be explained by the presence of clouds and/or hazes (as retrieved by, e.g. Barstow 2020, or simulated with 3D hydrodynamics-radiation model by, e.g. Steinrueck et al. 2021). As for future observations, Drummond et al. (2020) showed that according to the synthetic *JWST* and *Ariel* transmission observations (1 and 10 orbits, respectively), *JWST* and *Ariel* could resolve the aforementioned HD 189733b CH_4–NH_3 and CO_2 spectral features when provided with the data from our equilibrium and kinetics simulations. However, according to the synthetic *JWST* transmission spectrum, the NH_3 spectral feature at ∼10.5 μm could be obscured by the noise (Drummond et al. 2020, their fig. 12). Overall, it suggests that these telescopes could detect disequilibrium chemistry signatures due to CH_4–NH_3 and CO_2 in the HD 189733b transmission spectrum, if its atmosphere is cloud- and haze-free.

Synthetic HD 209458b transmission spectra (Figs 5c and 6c) from our equilibrium and kinetics simulations differ at several wavelengths, with the largest differences occurring at 4.1–4.5 μm and 10.2–11.3 μm. The primary cause of these differences is the transport-induced quenching of CH_4 and NH_3 (Drummond et al. 2020, and Section 3.3.2 in this work). In the region probed in transmission in the kinetics simulation, CH_4 abundance changes in a way that alters the pseudo-equilibrium between CO, H_2O, and CO_2, and leads to a decrease in CO_2 abundance at the western terminator, which, in turn, decreases the transit depth by up to 37 ppm at 4.1–4.5 μm in the kinetics simulation relative to the equilibrium one. Meanwhile, NH_3 abundance increases in the same region, more so at

high latitudes than at the equator, and causes an up to 75 ppm increase in the transit depth at 10.2–11.3 μm. Other differences between our spectra from kinetics and equilibrium simulations are mostly positive (up to 30 ppm), and are caused by changes in CH_4, NH_3, and HCN abundances, however, the contribution of these changes to the total transmission spectra is overwhelmed by the contribution of H_2O.

When compared to existing observations, our synthetic HD 209458b transmission spectra disagree with most of them, although there is substantial variation between the different observational studies. As for future observations, Drummond et al. (2020) showed that according to the synthetic *JWST* and *Ariel* transmission observations (1 and 10 orbits, respectively), *JWST* and *Ariel* could resolve the aforementioned HD 209458b's CO_2 spectral feature when provided with the data from our equilibrium and kinetics simulations. However, *JWST* could not resolve HD 209458b's NH_3 spectral feature at ∼10.5 μm well enough with one orbit (Drummond et al. 2020, their fig. 10). Overall, it means that these telescopes could detect a disequilibrium chemistry signature due to CO_2 in the HD 209458b transmission spectrum, if its atmosphere is cloud- and haze-free.

Synthetic WASP-17b transmission spectra (Figs 5d and 6d) from our equilibrium and kinetics simulations depart from each other the most at 4.3–4.4 μm and 10.2–11.3 μm. Similarly to HD 209458b, the cause of the first departure is the transport-induced quenching of CH_4, which by altering the pseudo-equilibrium between CO, H_2O, and CO_2, leads to a decrease in CO_2 abundance at the western terminator (Section 3.3.3), which, in turn, causes a decrease in the transit depth by up to 30 ppm in the kinetics simulation relative to the equilibrium one at these wavelengths. Also similarly to HD 209458b, NH_3 abundance increases in WASP-17b kinetics simulation, and causes up to a 20 ppm increase in the transit depth at 10.2–11.3 μm. Detecting these disequilibrium chemistry signatures in the WASP-17b's transmission spectrum might be challenging because of the signatures' small size, and the possibility of them to be muted if WASP-17b's atmosphere is not cloud- and haze-free. Other differences between our WASP-17b equilibrium and kinetics spectra are less than ±10 ppm.

When compared to existing observations, our synthetic WASP-17b transmission spectra broadly agree with observations by Sing et al. (2016) and Alderson et al. (2022). In fact, our simulations show that H_2O and CO_2 absorption are the main contributors to the total transmission spectra over the 2–30 μm range, which compares favourably with the detection of H_2O (at $>7\sigma$) and the inference of CO_2 (at $>3\sigma$) reported in the latter study. However, a further comparison with observations is required, e.g. with the upcoming *JWST* observations of WASP-17b transmission spectrum over the 0.6–14 μm range (*JWST* GTO-1353, PI: Nikole Lewis).

3.4.2 Emission spectrum

Following the methodology of Boutle et al. (2017), we calculate synthetic dayside emission spectra (Fig. 7) over the 2–30 μm range using the output from our equilibrium and kinetics simulations of the atmospheres of HAT-P-11b, HD 189733b, HD 209458b, and WASP-17b. Each synthetic emission spectrum shown here is the average of the spectra at two phase angles, when a maximum area of the planetary dayside is visible to the observer before and after the secondary eclipse. The observed secondary eclipse depth data were taken from the latest publications and observational data reviews, where possible, i.e. for HD 189733b, from Swain et al. (2009a, table 1), Charbonneau et al. (2008, table 1), Grillmair et al. (2008, fig. 1),
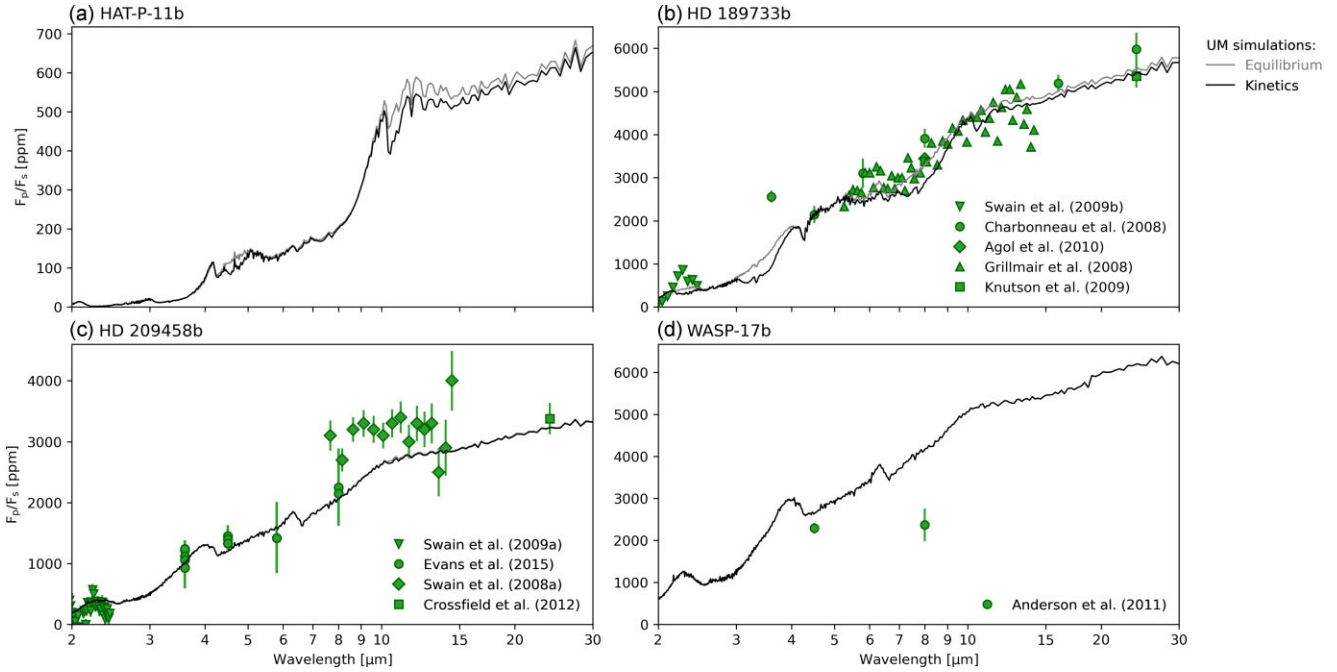
Figure 7. Dayside emission spectra from the equilibrium (grey dashed) and kinetics (black solid) simulations of HAT-P-11b (a), HD 189733b (b), HD 209458b (c), and WASP-17b (d). Grillmair et al. (2008) data were obtained using the WebPlotDigitizer.

Agol et al. (2010, section 6.7), and Knutson et al. (2009, table 1); for HD 209458b, from Swain et al. (2009b, fig. 3), Evans et al. (2015, table 4), Swain et al. (2008b, table 3), and Crossfield et al. (2012, table 5); and for WASP-17b, from Anderson et al. (2011, table 5).

Synthetic HAT-P-11b emission spectra (Fig. 7a) from our equilibrium and kinetics simulations differ at 4.3–5.0 and 10–30 μm. The difference at 4.3–5.0 μm is primarily caused by the transport-induced quenching of CO, while the difference at 10–30 μm is caused by the transport-induced quenching of NH_3 and a temperature decrease (Section 3.3.1) with respect to the equilibrium simulation. In the kinetics simulation, a planet-wide increase in CO and NH_3 mole fractions at the 4.5 and 10.5 μm photospheres, respectively, places these photospheres at lower pressures (Fig. C4), and thus lower temperatures (Fig. C5). This, in turn, causes the emergent intensity at the top of the atmosphere in the 4.5 and 10.5 μm spectral bands to decrease, and therefore reduce the planet-to-star flux ratios in the kinetics simulation relative to the equilibrium one. A decrease in temperature, caused by a decrease in the overall absorption due to a decrease in H_2O mole fractions at pressures lower than 1×10^4 Pa, additionally reduces the planet-to-star flux ratios at 10–30 μm in the kinetics simulation. However, because HAT-P-11b's atmosphere is the coldest relative to the other planetary atmospheres in our sample, the HAT-P-11b emission spectrum has the smallest planet-to-star flux ratios, which make its disequilibrium chemistry signatures due to CO, NH_3 and H_2O challenging to detect.

Synthetic HD 189733b emission spectra (Fig. 7b) from our equilibrium and kinetics simulations depart from each other at 2.1–2.5, 3.0–4.0, and 5.3–30.0 μm. In this case, the main cause of departure is the transport-induced quenching of CH_4 and NH_3 (Drummond et al. 2020, and Section 3.3.2 in this work). An increase in CH_4 mole fractions on the HD 189733b dayside in the kinetics simulation relative to the equilibrium one moves the 3.6 and 8.0 μm photospheres on the dayside to lower pressures and temperatures (Fig. C4 and C5), resulting in a decrease in the planet-to-star flux

ratios in the 3.6 and 8.0 μm spectral bands. Meanwhile, an increase in NH_3 mole fractions on the HD 189733b dayside in the kinetics simulation relative to the equilibrium one does not change the location of the 10.5 μm photosphere as much as the change in CH_4 does for the 3.6 and 8.0 μm photospheres, causing the emergent intensity at the top of the atmosphere to originate in a layer with relatively similar temperatures to those at chemical equilibrium. Yet, the resulting decrease in the planet-to-star flux ratio in the 10.5 μm spectral band in the kinetics simulation is comparable to those for CH_4 due to a high NH_3 absorption cross-section at the pressures and temperatures of the 10.5 μm photosphere (Fig. C6).

When compared to existing observations, our synthetic HD 189733b emission spectrum from the equilibrium simulation tends to agree more with observations by Swain et al. (2009a), Charbonneau et al. (2008), Grillmair et al. (2008), and Agol et al. (2010), but less so with observations by Knutson et al. (2009) at 24 μm than the kinetics simulation. This suggests that if the atmosphere of HD 189733b is cloud- and haze-free, it is closer to being at chemical equilibrium, or that our kinetics simulation misses some important processes, e.g. formation of clouds, which would generally increase the dayside planetary emission in the infrared part of the spectrum (Christie et al. 2021). As for future observations, Drummond et al. (2020) showed that according to the synthetic *JWST* and *Ariel* emission observations (1 and 5 orbits, respectively), *JWST* and *Ariel* could resolve the aforementioned HD 189733b CH_4 and NH_3 spectral features when provided with the data from our equilibrium and kinetics simulations (Drummond et al. 2020, their fig. 12). That suggests that these telescopes could detect disequilibrium chemistry signatures due to CH_4 and NH_3 in the HD 189733b emission spectrum, if its atmosphere is cloud- and haze-free.

Synthetic HD 209458b emission spectra (Fig. 7c) from our equilibrium and kinetics simulations differ at 10.2–10.8 μm. The main cause of this difference is the transport-induced quenching of
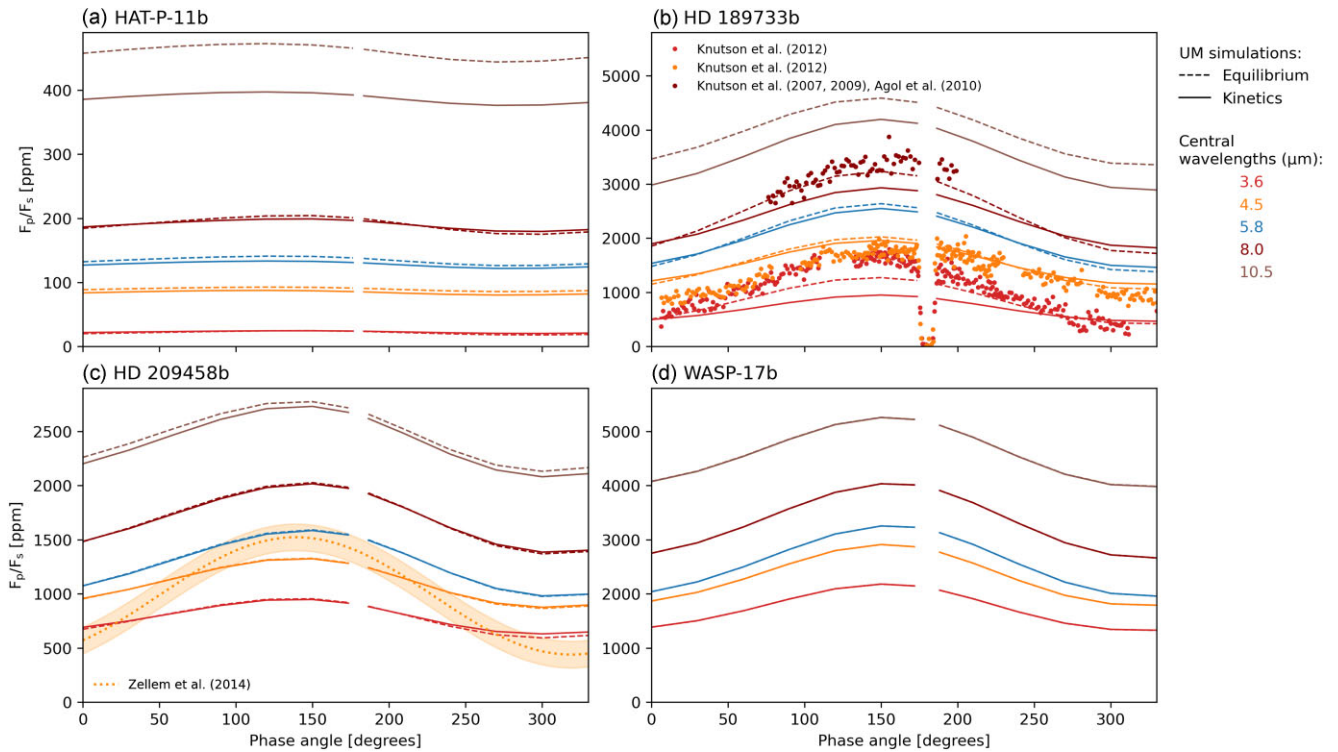
Figure 8. Emission phase curves from the equilibrium (dashed) and kinetics (solid) simulations of HAT-P-11b (a), HD 189733b (b), HD 209458b (c), and WASP-17b (d). The gap in the model data indicates the range of planetary phases when a planet is partially or fully eclipsed by its host star.

NH_3 (Drummond et al. 2020, and Section 3.3.2 in this work). In the kinetics simulation, NH_3 mole fractions increase on the dayside of HD 209458b 10.5 µm photosphere, moving this photosphere to slightly lower pressures and temperatures (Figs C4 and C5), and causing a small decrease in the planet-to-star flux ratios in the 10.5 µm spectral band in the kinetics simulation relative to the equilibrium one. HD 209458b's dayside CH_4 distribution at the 3.6 and 8.0 µm photospheres does change between equilibrium and kinetics simulations, but this change has a negligible effect on the planet-to-flux ratios in the 3.6 and 8.0 µm spectral bands.

When compared to existing observations, our synthetic HD 209458b emission spectra from both equilibrium and kinetics simulations agree reasonably well with observations presented in Swain et al. (2009b), Evans et al. (2015), and Crossfield et al. (2012), but similarly to the results of Amundsen et al. (2016) (their fig. 10) from their cloud- and haze-free HD 209458b UM simulation with the SOCRATES radiation scheme, and the analytical chemical scheme, our simulated planet-to-star flux ratios are smaller relative to those determined by Swain et al. (2008b). As for future observations, Drummond et al. (2020) showed that according to the synthetic *JWST* emission observations (1 orbit), *JWST* could not resolve the aforementioned HD 209458b NH_3 spectral features when provided with the data from our equilibrium and kinetics simulations (Drummond et al. 2020, their fig. 10). That suggests that *JWST* could not detect (at least with 1 orbit) a disequilibrium chemistry signature due to NH_3 in the HD 209458b emission spectrum, if its atmosphere is cloud- and haze-free.

Synthetic WASP-17b emission spectra (Fig. 7d) from our equilibrium and kinetics simulations are practically the same, suggesting that the emission spectrum of WASP-17b is not affected by transport-induced quenching (Section 3.3.3), as the emergent intensity at the top of its atmosphere originates in the part of the atmosphere that is at chemical equilibrium. The disagreement of both our simulations with the existing observations by Anderson et al. (2011) is intriguing, as it suggest that if WASP-17b atmosphere is cloud- and haze-free, our model misrepresents equilibrium chemistry (by assuming, e.g. lower than needed atmospheric metallicity), or misses some processes around the photosphere region. This makes the upcoming *JWST* observations of WASP-17b emission spectrum over the 0.6–14 µm range (*JWST* GTO-1353, PI: Nikole Lewis) even more welcome.

3.4.3 Phase curves

Following the methodology of Boutle et al. (2017), we calculate synthetic emission phase curves (Fig. 8) using the output from our equilibrium and kinetics simulations of the atmospheres of HAT-P-11b, HD 189733b, HD 209458b, and WASP-17b. Each synthetic emission phase curve shown here is comprised of the ratios of planetary to stellar flux summed over the range of SOCRATES spectral bands falling within the corresponding *Spitzer*/IRAC 3.6, 4.5, 5.8, and 8.0 µm bandpasses[11], with the exception of 10.5 µm, for which we considered only a single SOCRATES spectral band[12].

---

[11] IRAC Instrument Handbook: Spectral Response (https://irsa.ipac.caltech.edu/data/SPITZER/docs/irac/calibrationfiles/spectralresponse/).

[12] Spectral band centre (in µm), the corresponding *Spitzer*/IRAC wavelength bandpass bounds (in µm), and the number of SOCRATES spectral bands falling within each considered bandpass:

(i) 3.6 µm (3.08106, 4.01038) 76,
(ii) 4.5 µm (3.72249, 5.22198) 78,
(iii) 5.8 µm (4.74421, 6.62251) 60,
(iv) 8.0 µm (6.15115, 9.72875) 60,
(v) 10.5 µm (10.416666555101983, 10.52631614584243) 1.

The observed phase curve data for HD 189733b at 3.6 and 4.5 μm were taken from Knutson et al. (2012), and at 8 μm from Knutson et al. (2007, 2009), and Agol et al. (2010), while the data for HD 209458b at 4.5 μm were taken from Zellem et al. (2014).

Synthetic HAT-P-11b phase curves (Fig. 8a) vary little with phase angle, as is expected due to small thermal and chemical gradients predicted for this planet. However, its phase curves still differ between simulations. In the 4.5, 5.8, and 10.5 μm bandpasses, phase curves from the kinetics simulation are offset from those from the equilibrium simulation. In the case of 4.5 and 10.5 μm, the offset is caused by the transport-induced quenching (Section 3.3.1), which by increasing CO and NH_3 abundances in a way that evens out their spatial gradients moves the 4.5 and 10.5 μm photospheres to lower pressures and temperatures, and decreases planet-to-star flux ratios in these bandpasses. In the case of 5.8 μm, however, the offset occurs not because of the transport-induced quenching, but because of a temperature decrease. This decrease in temperature is caused by a decrease in H_2O abundance at pressures lower then those of the 5.8 μm photosphere, which reduces the overall absorption at these pressures, thus reducing the temperature. Lastly, the 3.6 and 8.0 μm phase curves from both equilibrium and kinetics simulations are similar, because CH_4 abundance does not change much between simulations.

Synthetic HD 189733b phase curves (Fig. 8b) vary more with phase angle than those of HAT-P-11b and HD 209458b. While both HD 189733b simulations predict a large day-night thermal gradient, the kinetics simulation predicts smaller chemical gradients, and thus smaller phase curve amplitudes. In the 3.6, 4.5, 5.8, and 8.0 μm bandpasses, planet-to-star flux ratios decrease on the dayside but increase on the nightside in the kinetics simulation relative to the equilibrium one. In the case of 3.6, 5.8, and 8.0 μm, the differences are caused by the transport-induced quenching (Section 3.3.2), which by smoothing CH_4 and H_2O abundance gradients with longitude flattens phase curves in these bandpasses. In the case of 4.5 μm, however, the cause is a combination of changes in abundances of CO, H_2O, and CO_2, with an increase in H_2O on the dayside overpowering the contributions from other gases and causing the reduction in flux on the dayside, and a decrease in H_2O and CO_2 on the nightside controlling the increase in flux on the nightside. Lastly, the 10.5 μm phase curve from the kinetics simulation shows consistently lower planet-to-star flux ratios than the equilibrium simulation because of a higher predicted NH_3 abundance.

Comparison of our synthetic HD 189733b phase curves with existing observations produces mixed results. The observed 3.6 and 4.5 μm phase curves show similar fluxes before the eclipse (0–180°) but different fluxes after the eclipse (180–360°). Our synthetic 3.6 and 4.5 μm phase curves, however, are offset from each other at all phase angles, which agrees with observations after the eclipse but overestimates them at 3.6 μm and underestimates them at 4.5 μm before the eclipse. If we compare the 3.6 and 8.0 μm phase curves, phase curves from our equilibrium simulation tend to agree more with observations than those from our kinetics simulation. This suggests that if HD 189733b atmosphere is cloud- and haze-free, it is closer to being at chemical equilibrium. In fact, if we update our reduced chemical network from that of Venot et al. (2019) to that of Venot et al. (2020), it will likely increase CH_4 abundance while keeping CO abundance the same in our kinetics simulation (see HD 189733b case in Venot et al. 2020, their fig. 2). That would, in turn, reduce the fluxes the 3.6 and 8.0 μm bandpasses in our kinetics simulation even more, and worsen the agreement with the observed 3.6 and 8.0 μm phase curves. Therefore, an alternative direction of model

development might be required to improve the agreement between observations and the UM in the case of HD 189733b, e.g. coupling a gas-phase chemistry scheme to a cloud/haze scheme.

Synthetic HD 209458b phase curves (Fig. 8c) from our equilibrium and kinetics simulations differ in the 3.6 and 8.0 μm bandpasses at phase angles corresponding to the nightside, and are offset from each other in the 10.5 μm band. The cause of these differences is the transport-induced quenching (Section 3.3.2), which by increasing CH_4 abundance on the dayside but decreasing it on the nightside flattens phase curves in the 3.6 and 8.0 μm bandpasses, while a planet-wide increase in NH_3 abundance decreases planet-to-star flux ratios in the 10.5 μm band in the kinetics simulation relative to the equilibrium one.

When compared to the fit to phase curve observations in the 4.5 μm bandpass (Zellem et al. 2014), both HD 209458b simulations underestimate the observed phase curve amplitude by underestimating the flux on the dayside and overestimating the flux on the nightside. Biases such as these, typical for cloud-free models (e.g. Parmentier & Crossfield 2018), could be improved upon by including clouds (Parmentier, Showman & Fortney 2021). This was done for HD 209458b with the UM by Christie et al. (2021), who found that all cloud treatments they considered increase their predicted 4.5 μm phase curve amplitude (their fig. 14), but some discrepancies between observations and the model remain.

Synthetic WASP-17b phase curves (Fig. 8d) vary with phase angle in a similar way as phase curves from our HD 189733b equilibrium simulation. However, in contrast to the other three planets in our sample, WASP-17b's phase curves from both simulations are the same in each considered bandpass, largely because the photospheres corresponding to the centre of each bandpass are located in the region of WASP-17b atmosphere that is at chemical equilibrium (Section 3.3.3).

4 DISCUSSION

Transport-induced quenching plays an important role in controlling the chemical composition of the atmospheres of HAT-P-11b, HD 189733b, HD 209458b, and WASP-17b. However, how critical this role is in shaping their synthetic spectra and phase curves varies from planet to planet. By expanding the stellar-planetary parameter space explored with our model using both chemical equilibrium and chemical kinetics schemes, we show that transport-induced quenching is predicted to occur in atmospheres of both newly considered planets, a smaller and colder HAT-P-11b and a hotter and larger WASP-17b relative to previously simulated HD 189733b and HD 209458b (Drummond et al. 2020). Yet, when we compare the results for all four planets, the largest differences between synthetic observations produced using our equilibrium and kinetics simulations occur for HD 189733b. It means that there seems to be a 'sweet spot' combination of stellar and planetary parameters that facilitates the formation of signatures of transport-induced quenching. For the HD 189733 system, such a combination causes our HD 189733b cloud- and haze-free kinetics simulation to have an atmospheric circulation that develops the deepest equatorial jet, and a thermal structure that supports deep quenching, which due to a large contribution from meridional quenching helps shift the photosphere drastically up into the region of lower temperatures. The existence of this 'sweet spot' emerges as a balance between the time-scales of advection and chemistry. In other words, and if we consider the planetary temperature only, to maintain efficient transport-induced quenching, this temperature needs to be low enough to allow a long enough chemical time-scale, but high enough so that the

Table 3. Observability of signatures of transport-induced quenching. □ signifies the absence or little difference between predictions from our equilibrium and kinetics simulations, ■ indicates the presence of a substantial difference, and the fact that it is potentially detectable with *JWST* (T1) or *Ariel* (T2), ⊞ highlights cases where the difference in predicted chemical species abundances is noticeable but unclear if it is detectable, – indicates that no information is available.

Planet	Species	Transit			Eclipse			Phase curve	
		UM	T1	T2	UM	T1	T2	UM	
HAT-P-11b	CH_4	□	–	–	□	–	–	□	– –
	CO	■	–	–	■	–	–	■	– –
	CO_2	□	–	–	□	–	–	□	– –
	H_2O	□	–	–	■	–	–	■	– –
	HCN	□	–	–	□	–	–	□	– –
	NH_3	■	–	–	■	–	–	■	– –
HD 189733b	CH_4	■	■	■	■	■	■	■	– –
	CO	□	□	□	□	□	□	■	– –
	CO_2	■	□	□	□	□	□	■	– –
	H_2O	□	□	□	□	□	□	■	– –
	HCN	□	□	□	□	□	□	□	– –
	NH_3	■	⊞	–	■	■	–	■	– –
HD 209458b	CH_4	□	□	□	□	□	□	□	– –
	CO	□	□	□	□	□	□	□	– –
	CO_2	■	■	■	□	□	□	□	– –
	H_2O	□	□	□	□	□	□	□	– –
	HCN	□	□	□	□	□	□	□	– –
	NH_3	■	⊞	–	■	■	–	■	– –
WASP-17b	CH_4	□	–	–	□	–	–	□	– –
	CO	□	–	–	□	–	–	□	– –
	CO_2	■	–	–	□	–	–	□	– –
	H_2O	□	–	–	□	–	–	□	– –
	HCN	□	–	–	□	–	–	□	– –
	NH_3	■	–	–	□	–	–	□	– –

thermal gradient between the irradiated hot dayside and the dark cold nightside could sustain a short enough advection time-scale.

The observability and detectability of the 'sweet spot' of transport-induced quenching currently relies heavily on the assumption of a cloud- and haze-free atmosphere. By comparing our model predictions with existing observations, we show that the synthetic observations produced using our kinetics simulations do not necessarily agree better with observations than those produced using our equilibrium simulations. However, the differences in predicted synthetic observations between these simulations (except for WASP-17b emission spectrum and phase curves) are large enough to be identifiable as signatures of transport-induced quenching, and even be detectable with *JWST* and *Ariel* (Table 3), assuming the atmospheres are cloud- and haze-free.

Lastly, and despite that our sample of planets is small, we would like to report evidence for the trend in chemical abundances that depends on the effective planetary temperature. In our equilibrium and kinetics simulations, CH_4, H_2O, NH_3, and HCN decrease, CO_2 stays relatively constant and CO increases with increasing effective planetary temperature. This agrees with the results of Baeyens et al. (2021) from a relevant subset of pseudo-2D chemical kinetics simulations of planets with 800–1600 K effective planetary temperature rotating around K5, G5, and F5 stars (their figs 8 and E9).

5 CONCLUSIONS

We present results from a set of cloud- and haze-free simulations of the atmospheres of HAT-P-11b, HD 189733b, HD 209458b, and WASP-17b computed using a coupled 3D hydrodynamics-radiation-chemistry model, the UM. This work expands the stellar-planetary parameter space explored with the UM relative to the similar previous work of Drummond et al. (2020).

We conclude that according to our equilibrium and kinetics simulations:

(i) Transport-induced quenching occurs in atmospheres of all planets considered in our work, however, the extent to which transport-induced quenching affects their synthetic observations varies from planet to planet.

(ii) Due to a combination of stellar and planetary parameters, HD 189733b's atmosphere develops a particular balance between its advection and chemistry time-scales, that places it at the 'sweet spot' for identification of signatures of transport-induced quenching.

(iii) However, this 'sweet spot' emerges when we assume a cloud- and haze-free atmosphere, which might be a good assumption for some planets, e.g. WASP-96b (Nikolov et al. 2018, 2022), making such planets the best targets for testing this theory, but when it is not a fair assumption, the observability and detectability of signatures of transport-induced quenching should be re-evaluated by taking into account processes that affect them.

5.1 Future work

The potential to detect signatures of disequilibrium chemistry in general is likely to be larger when both transport-induced quenching and another disequilibrium process, photochemistry (Moses 2014), are considered together. Photochemistry was shown to have an impact on the gas-phase composition of H_2-dominated atmospheres both experimentally (Fleury et al. 2019, 2020) and through modelling (most recently by Baeyens et al. 2022). While Baeyens et al. (2022) found that photochemistry has a limited impact on the synthetic

transmission spectra of tidally locked H_2-dominated planets, they considered photochemistry in isolation from photochemical hazes. Pathways of formation of photochemical hazes in atmospheres of warm and hot Jupiters are not yet known, as laboratory data for the relevant gas mixtures and temperatures have only recently started to be obtained (Fleury et al. 2019; He et al. 2020). However, formation of aerosols (hazes particles) from initial gas mixtures without the need for artificial nucleation centres was reported already, which confirms the existence of a transition from gas-phase only homogeneous chemistry to gas-solid heterogeneous chemistry in such regimes. This highlights the need for a good representation of (1) chemistry in the absence of light (i.e. without an interaction with a photon), (2) photochemistry (i.e. with an interaction with a photon), (3) transformation of gas into solid, and (4) gas-solid heterogeneous chemistry. Given the complexity of photochemical haze formation and computational expense of 3D modelling, in the short-term we plan to address (1) by implementing the update to the methanol chemistry recommended for warm Neptune simulations by Venot et al. (2020) and/or use the Tsai, Lee & Pierrehumbert (2022) chemical network, and (2) by leveraging the work done by Ridgway et al. (2023), who added the treatment of photodissociation reactions into the UM, leaving (3) and (4) for the medium- to long-term.

Another medium- to long-term goal is to couple the UM's chemical kinetics scheme to a cloud formation scheme. Previously, the UM's analytic chemical scheme based on Burrows & Sharp (1999) had been coupled by Lines et al. (2018b) to the kinetic, microphysical mineral cloud formation model of Lee et al. (2016) and by Lines et al. (2019) and Christie et al. (2021, 2022) to the EDDYSED cloud model of Ackerman & Marley (2001). Coupling the UM's chemical kinetics scheme to any cloud scheme would require an extension of the chemical network to include cloud forming species relevant for H_2-dominated atmospheres.

Lastly, according to our simulations, transport-induced quenching occurs deep within the atmospheres of HAT-P-11b and HD 189733b. It suggests that capturing interactions between the planetary interior and the atmosphere above is likely to be particularly important for these two planets, and we would like to simulate that part of the atmosphere better in the future.

Software. Material produced using Met Office Software. The scripts to process and visualize the Met Office UNIFIED MODEL data are available on GitHub at https://github.com/mzamyatina/sign atures_of_wind_driven_chemistry_on_hot_jupiters; these scripts are dependent on the following PYTHON libraries: AEOLUS (Sergeev & Zamyatina 2022), IRIS (MetOffice 2022), IPYTHON (Perez & Granger 2007), JUPYTER (Kluyver et al. 2016), NUMPY (Harris et al. 2020), PANDAS (McKinney 2010), and MATPLOTLIB (Hunter 2007).

We would also like to note the energy intensive nature of supercomputing, especially simulations with interactive chemistry. We estimate the final production runs needed for this paper resulted in roughly 4.5 tCO$_2$e emitted into the atmosphere.

DATA AVAILABILITY

The research data supporting this publication are openly available from the Open Research Exeter (ORE) online repository at: https://doi.org/10.24378/exe.4304. For the purpose of open access, the authors have applied a Creative Commons Attribution (CC BY) licence to any Author Accepted Manuscript version arising.

REFERENCES

Ackerman A. S., Marley M. S., 2001, ApJ, 556, 872

Agol E., Cowan N. B., Knutson H. A., Deming D., Steffen J. H., Henry G. W., Charbonneau D., 2010, ApJ, 721, 1861

Agúndez M., Venot O., Iro N., Selsis F., Hersant F., Hébrard E., Dobrijevic M., 2012, A&A, 548, A73

Agúndez M., Parmentier V., Venot O., Hersant F., Selsis F., 2014, A&A, 564, A73

Ahrer E., Wheatley P. J., Kirk J., Gandhi S., King G. W., Louden T., 2022, MNRAS, 510, 4857

Alam M. K. et al., 2021, ApJL, 906, L10

Alderson L. et al., 2022, MNRAS, 512, 4185

Allard N. F., Royer A., Kielkopf J. F., Feautrier N., 1999, Phys. Rev. A, 60, 1021

Allard N. F., Allard F., Hauschildt P. H., Kielkopf J. F., Machin L., 2003, A&A, 411, L473

Allard N. F., Spiegelman F., Kielkopf J. F., 2007, A&A, 465, 1085

Amundsen D. S., Baraffe I., Tremblin P., Manners J., Hayek W., Mayne N. J., Acreman D. M., 2014, A&A, 564, A59

Amundsen D. S. et al., 2016, A&A, 595, A36

Amundsen D. S., Tremblin P., Manners J., Baraffe I., Mayne N. J., 2017, A&A, 598, A97

Anderson D. R. et al., 2010, ApJ, 709, 159

Anderson D. R. et al., 2011, MNRAS, 416, 2108

Asplund M., Grevesse N., Sauval A. J., Scott P., 2009, ARA&A, 47, 481

Baeyens R., Decin L., Carone L., Venot O., Agúndez M., Mollière P., 2021, MNRAS, 505, 5603

Baeyens R., Konings T., Venot O., Carone L., Decin L., 2022, MNRAS, 512, 4877

Bakos G. Á. et al., 2010, ApJ, 710, 1724

Barber R. J., Tennyson J., Harris G. J., Tolchenov R. N., 2006, MNRAS, 368, 1087

Barber R. J., Strange J. K., Hill C., Polyansky O. L., Mellau G. C., Yurchenko S. N., Tennyson J., 2014, MNRAS, 437, 1828

Barstow J. K., 2020, MNRAS, 497, 4183

BelBruno J. J., Gelfand J., Radigan W., Verges K., 1982, J. Mol. Spectrosc., 94, 336

Boutle I. A., Mayne N. J., Drummond B., Manners J., Goyal J., Hugo Lambert F., Acreman D. M., Earnshaw P. D., 2017, A&A, 601, A120

Burrows A., Sharp C. M., 1999, ApJ, 512, 843

Caffau E., Ludwig H.-G., Steffen M., Freytag B., Bonifacio P., 2011, Sol. Phys., 268, 255

Chachan Y. et al., 2019, AJ, 158, 244

Charbonneau D., Knutson H. A., Barman T., Allen L. E., Mayor M., Megeath S. T., Queloz D., Udry S., 2008, ApJ, 686, 1341

Charnay B. et al., 2022, Exp. Astron., 53, 417

Christie D. A. et al., 2021, MNRAS, 506, 4500

Christie D. A., Mayne N. J., Gillard R. M., Manners J., Hébrard E., Lines S., Kohary K., 2022, MNRAS, 517, 1407

Cooper C. S., Showman A. P., 2006, ApJ, 649, 1048

Crossfield I. J. M., Knutson H., Fortney J., Showman A. P., Cowan N. B., Deming D., 2012, ApJ, 752, 81

Dobbs-Dixon I., Cowan N. B., 2017, ApJL, 851, L26

Drummond B., Tremblin P., Baraffe I., Amundsen D. S., Mayne N. J., Venot O., Goyal J., 2016, A&A, 594, A69

Drummond B., Mayne N. J., Baraffe I., Tremblin P., Manners J., Amundsen D. S., Goyal J., Acreman D., 2018a, A&A, 612, A105

Drummond B. et al., 2018b, ApJL, 855, L31

Drummond B., Mayne N. J., Manners J., Baraffe I., Goyal J., Tremblin P., Sing D. K., Kohary K., 2018c, ApJ, 869, 28

Drummond B. et al., 2020, A&A, 636, A68

Edwards J. M., 1996, J. Atmos. Sci., 53, 1921

Edwards J. M., Slingo A., 1996, Q. J. R. Meteorol. Soc., 122, 689

Evans T. M., Aigrain S., Gibson N., Barstow J. K., Amundsen D. S., Tremblin P., Mourier P., 2015, MNRAS, 451, 680

Fleury B., Gudipati M. S., Henderson B. L., Swain M., 2019, ApJ, 871, 158

Fleury B., Gudipati M. S., Henderson B. L., Swain M., 2020, ApJ, 899, 147

Fraine J. et al., 2014, Nature, 513, 526

Gamache R. R., Lynch R., Brown L. R., 1996, J. Quant. Spectrosc. Radiat. Transfer, 56, 471

Goyal J. M., Wakeford H. R., Mayne N. J., Lewis N. K., Drummond B., Sing D. K., 2019, MNRAS, 482, 4503

Goyal J. M. et al., 2020, MNRAS, 498, 4680

Greene T. P., Line M. R., Montero C., Fortney J. J., Lustig-Yaeger J., Luther K., 2016, ApJ, 817, 17

Grillmair C. J. et al., 2008, Nature, 456, 767

Hadded S., Aroui H., Orphal J., Bouanich J. P., Hartmann J. M., 2001, J. Mol. Spectrosc., 210, 275

Harris G. J., Tennyson J., Kaminsky B. M., Pavlenko Ya. V., Jones H. R. A., 2006, MNRAS, 367, 400

Harris C. R. et al., 2020, Nature, 585, 357

He C. et al., 2020, Planet. Sci. J., 1, 51

Heiter U. et al., 2008, J. Phys.: Conf. Ser., 130, 012011

Heiter U. et al., 2015, Phys. Scr., 90, 054010

Hindmarsh A. C., 1983, in Stepleman R. S., ed., Scientific Computing. North-Holland, Amsterdam, p. 55

Howell S. B., 2020, Front. Astron. Space Sci., 7, 1

Hunter J. D., 2007, Comput. Sci. Eng., 9, 90

Irwin P. G. J., Parmentier V., Taylor J., Barstow J., Aigrain S., Lee G. K., Garland R., 2020, MNRAS, 493, 106

Kataria T., Sing D. K., Lewis N. K., Visscher C., Showman A. P., Fortney J. J., Marley M. S., 2016, ApJ, 821, 9

Kluyver T. et al., 2016, in Loizides F., Scmidt B., eds, Positioning and Power in Academic Publishing: Players, Agents and Agendas – Proceedings of the 20th International Conference on Electronic Publishing, ELPUB 2016. IOS Press, p. 87

Knutson H. A. et al., 2007, Nature, 447, 183

Knutson H. A. et al., 2009, ApJ, 690, 822

Knutson H. A. et al., 2012, ApJ, 754, 22

Kreidberg L., 2018, Handbook of Exoplanets. Springer, Cham

Landrain V., Blanquet G., Lepère M., Walrand J., Bouanich J. P., 1997, J. Mol. Spectrosc., 182, 184

Le Moal M. F., Severin F., 1986, J. Quant. Spectrosc. Radiat. Transfer, 35, 145

Lee G., Dobbs-Dixon I., Helling Ch., Bognar K., Woitke P., 2016, A&A, 594, A48

Line M. R., Parmentier V., 2016, ApJ, 820, 78

Lines S. et al., 2018a, MNRAS, 481, 194

Lines S. et al., 2018b, A&A, 615, A97

Lines S., Mayne N. J., Manners J., Boutle I. A., Drummond B., Mikal-Evans T., Kohary K., Sing D. K., 2019, MNRAS, 488, 1332

Louden T., Wheatley P. J., 2015, ApJL, 814, L24

MacDonald R. J., Goyal J. M., Lewis N. K., 2020, ApJL, 893, L43

McKinney W., 2010, in van der Walt S., Millman J., eds, Proceedings of the 9th Python in Science Conference, Austin, Texas, p. 56

Mantz A. W., Malathy Devi V., Chris Benner D., Smith M. A. H., Predoi-Cross A., Dulick M., 2005, J. Mol. Struct., 742, 99

Margolis J. S., 1993, J. Quant. Spectrosc. Radiat. Transfer, 50, 431

Mayne N. J., Baraffe I., Acreman D. M., Smith C., Wood N., Amundsen D. S., Thuburn J., Jackson D. R., 2014a, Geosci. Model Dev., 7, 3059

Mayne N. J. et al., 2014b, A&A, 561, A1

Mayne N. J. et al., 2017, A&A, 604, A79

Mayne N. J., Drummond B., Debras F., Jaupart E., Manners J., Boutle I. A., Baraffe I., Kohary K., 2019, ApJ, 871, 56

Mendonça J. M., Tsai S.-M., Malik M., Grimm S. L., Heng K., 2018, ApJ, 869, 107

MetOffice, 2022, Iris: A Python library for analysing and visualising meteorological and oceanographic data sets

Moses J. I., 2014, Phil. Trans. R. Soc. A, 372

Moses J. I. et al., 2011, ApJ, 737, 15

Moses J. I. et al., 2013, ApJ, 777, 34

Moses J. I., Tremblin P., Venot O., Miguel Y., 2022, Exp. Astron., 53, 279

Nikolov N. et al., 2018, Nature, 557, 526

Nikolov N. K. et al., 2022, MNRAS, 515, 3037

Nouri S., Orphal J., Aroui H., Hartmann J.-M., 2004, J. Mol. Spectrosc., 227, 60

Padmanabhan A., Tzanetakis T., Chanda A., Thomson M. J., 2014, J. Quant. Spectrosc. Radiat. Transfer, 133, 81

Parmentier V., Crossfield I. J., 2018, Handbook of Exoplanets. Springer, Cham

Parmentier V., Showman A. P., Fortney J. J., 2021, MNRAS, 501, 78

Perez F., Granger B. E., 2007, Comput. Sci. Eng., 9, 21

Pine A. S., 1992, J. Chem. Phys., 97, 773

Pine A. S., Markov V. N., Buffa G., Tarrini O., 1993, J. Quant. Spectrosc. Radiat. Transfer, 50, 337

Pluriel W., Zingales T., Leconte J., Parmentier V., 2020, A&A, 636, A66

Pont F., Sing D. K., Gibson N. P., Aigrain S., Henry G., Husnoo N., 2013, MNRAS, 432, 2917

Prinn R. G., Barshay S. S., 1977, Science, 198, 1031

Rajpurohit A. S., Reylé C., Allard F., Homeier D., Schultheis M., Bessell M. S., Robin A. C., 2013, A&A, 556, A15

Régalia-Jarlot L., Thomas X., von der Heyden P., Barbe A., 2005, J. Quant. Spectrosc. Radiat. Transfer, 91, 121

Richard C. et al., 2012, J. Quant. Spectrosc. Radiat. Transfer, 113, 1276

Ridgway R. J. et al., 2023, MNRAS, 518, 2472

Roman M. T., Kempton E. M.-R., Rauscher E., Harada C. K., Bean J. L., Stevenson K. B., 2021, ApJ, 908, 101

Rothman L. S. et al., 2009, J. Quant. Spectrosc. Radiat. Transfer, 110, 533

Rothman L. S. et al., 2010, J. Quant. Spectrosc. Radiat. Transfer, 111, 2139

Ryabchikova T., Piskunov N., Kurucz R. L., Stempels H. C., Heiter U., Pakhomov Yu., Barklem P. S., 2015, Phys. Scr., 90, 054005

Sainsbury-Martinez F. et al., 2019, A&A, 632, A114

Saumon D., Marley M. S., Lodders K., Freedman R. S., 2003, in Martín E., ed., Proc. IAU Symp. 211, Brown Dwarfs. Astron. Soc. Pac., San Francisco, p. 345

Sauval A. J., Tatum J. B., 1984, ApJS, 56, 193

Sergeev D. E., Zamyatina M., 2022, aeolus

Sharp C. M., Burrows A., 2007, ApJS, 168, 140

Sheppard K. B. et al., 2021, AJ, 161, 51

Showman A. P., Lewis N. K., Fortney J. J., 2015, ApJ, 801, 95

Sing D. K., Désert J.-M., Lecavelier Des Etangs A., Ballester G. E., Vidal-Madjar A., Parmentier V., Hebrard G., Henry G. W., 2009, A&A, 505, 891

Sing D. K. et al., 2016, Nature, 529, 59

Skemer A. J. et al., 2014, ApJ, 792, 17

Snellen I. A. G., de Kok R. J., de Mooij E. J. W., Albrecht S., 2010, Nature, 465, 1049

Solodov A. M., Starikov V. I., 2009, Mol. Phys., 107, 43

Southworth J., 2011, MNRAS, 417, 2166

Steinrueck M. E., Parmentier V., Showman A. P., Lothringer J. D., Lupu R. E., 2019, ApJ, 880, 14

Steinrueck M. E., Showman A. P., Lavvas P., Koskinen T., Tan X., Zhang X., 2021, MNRAS, 504, 2783

Steyert D. W., Wang W. F., Sirota J. M., Donahue N. M., Reuter D. C., 2004, J. Quant. Spectrosc. Radiat. Transfer, 83, 183

Swain M. R., Vasisht G., Tinetti G., 2008a, Nature, 452, 329

Swain M. R., Bouwman J., Akeson R. L., Lawler S., Beichman C. A., 2008b, ApJ, 674, 482

Swain M. R., Vasisht G., Tinetti G., Bouwman J., Chen P., Yung Y., Deming D., Deroo P., 2009a, ApJ, 690, L114

Swain M. R. et al., 2009b, ApJ, 704, 1616

Tashkun S. A., Perevalov V. I., 2011, J. Quant. Spectrosc. Radiat. Transfer, 112, 1403

Tennyson J. et al., 2016, J. Mol. Spectrosc., 327, 73

Thibault F., Boissoles J., Le Doucen R., Bouanich J. P., Arcas P., Boulet C., 1992, J. Chem. Phys., 96, 4945

Thibault F., Calil B., Boissoles J., Launay J. M., 2000, Phys. Chem. Chem. Phys., 2, 5404

Tinetti G. et al., 2018, Exp. Astron., 46, 135

Tremblin P. et al., 2017, ApJ, 841, 30

Tsai S.-M., Kitzmann D., Lyons J. R., Mendonça J., Grimm S. L., Heng K., 2018, ApJ, 862, 31

Tsai S.-M., Lee E. K. H., Pierrehumbert R., 2022, A&A, 664, A82

Varanasi P., Chudamani S., 1990, J. Quant. Spectrosc. Radiat. Transfer, 43, 1

Venot O., Hébrard E., Agúndez M., Dobrijevic M., Selsis F., Hersant F., Iro N., Bounaceur R., 2012, A&A, 546, A43

Venot O., Bounaceur R., Dobrijevic M., Hébrard E., Cavalié T., Tremblin P., Drummond B., Charnay B., 2019, A&A, 624, A58

Venot O., Cavalié T., Bounaceur R., Tremblin P., Brouillard L., Ben Brahim R. L., 2020, A&A, 634, A78

Visscher C., Moses J. I., 2011, ApJ, 738, 72

Wakeford H. R. et al., 2018, AJ, 155, 29

Wakelam V., KIDA Team, 2012, Kinetic Database for Astrochemistry, Vol. 58, EAS Publications Series. European Conference on Laboratory Astrophysics, p. 287

Wood N. et al., 2014, Q. J. R. Meteorol. Soc., 140, 1505

Wyttenbach A., Ehrenreich D., Lovis C., Udry S., Pepe F., 2015, A&A, 577, A62

Yurchenko S. N., Tennyson J., 2014, MNRAS, 440, 1649

Yurchenko S. N., Barber R. J., Tennyson J., 2011, MNRAS, 413, 1828

Zahnle K. J., Marley M. S., 2014, ApJ, 797, 41

Zellem R. T. et al., 2014, ApJ, 790, 53

APPENDIX A: LINE LISTS

Table A1. Line lists and partition functions used in this work. More details can be found in Goyal et al. (2020).

Species	Line list	Partition function
Li	VALD3[a]	Sauval & Tatum (1984)
Na	VALD3[a]	Sauval & Tatum (1984)
K	VALD3[a]	Sauval & Tatum (1984)
Rb	VALD3[a]	Sauval & Tatum (1984)
Cs	VALD3[a]	Sauval & Tatum (1984)
H_2O	Barber et al. (2006)	Barber et al. (2006)
CO	Rothman et al. (2010)	Rothman et al. (2009)
CO_2	Tashkun & Perevalov (2011)	Rothman et al. (2009)
CH_4	Yurchenko & Tennyson (2014)	Yurchenko & Tennyson (2014)
NH_3	Yurchenko, Barber & Tennyson (2011)	Sauval & Tatum (1984)
HCN	Harris et al. (2006), Barber et al. (2014)	Harris et al. (2006), Barber et al. (2014)
H_2-H_2 CIA	Richard et al. (2012)	N/A
H_2-He CIA	Richard et al. (2012)	N/A

Note. [a]Heiter et al. (2008), Heiter et al. (2015), Ryabchikova et al. (2015) (http://vald.astro.uu.se/~vald/php/vald.php).

Table A2. Pressure broadening data used in this work. More details can be found in Goyal et al. (2020).

Species	Broadener	Line width	Exponent
Li, Rb, Cs	H_2	Allard et al. (1999)	Sharp & Burrows (2007)
	He	Allard et al. (1999)	Sharp & Burrows (2007)
Na, K	H_2	Allard et al. (1999), Allard et al. (2003), Allard, Spiegelman & Kielkopf (2007)	Sharp & Burrows (2007)
	He	Allard et al. (1999), Allard et al. (2003), Allard et al. (2007)	Sharp & Burrows (2007)
H_2O	H_2	Gamache, Lynch & Brown (1996)	Gamache et al. (1996)
	He	Solodov & Starikov (2009), Steyert et al. (2004)	Gamache et al. (1996)
CO	H_2	Régalia-Jarlot et al. (2005)	Le Moal & Severin (1986)
	He	BelBruno et al. (1982), Mantz et al. (2005)	Mantz et al. (2005)
CO_2	H_2	Padmanabhan et al. (2014)	Sharp & Burrows (2007)
	He	Thibault et al. (1992)	Thibault et al. (2000)
CH_4	H_2	Pine (1992), Margolis (1993)	Margolis (1993)
	He	Pine (1992)	Varanasi & Chudamani (1990)
NH_3	H_2	Hadded et al. (2001), Pine et al. (1993)	Nouri et al. (2004)
	He	Hadded et al. (2001), Pine et al. (1993)	Sharp & Burrows (2007)
HCN	H_2	Landrain et al. (1997)	Sharp & Burrows (2007)
	He	Landrain et al. (1997)	Sharp & Burrows (2007)

## APPENDIX B: MODEL PSEUDO-STEADY STATE

To check if the model has reached a steady state, we analysed the evolution of (a) the global maximum wind velocities (Fig. B1), (b) the global mean top-of-atmosphere net energy flux (Fig. B2), and (c) the total mass of major opacity sources, CH_4, CO, CO_2, H_2O, HCN, and NH_3 (Fig. B3). These quantities serve as metrics of the dynamical, radiative, and chemical state of the atmosphere, and no change in these metrics with time indicates that the atmosphere has reached a steady state.

The global maximum zonal, meridional, and vertical wind velocities reach 2.6, 1.4, and 0.005 $km\,s^{-1}$, respectively, for HAT-P-11b, 6.9, 3.5, and 0.01 $km\,s^{-1}$ for HD 189733b, 6.5, 2.7, and 0.02 $km\,s^{-1}$ for HD 209458b, and 6.9, 2.5, and 0.05 $km\,s^{-1}$ for WASP-17b, and change by less than 1 per cent over the last 200 d. The global mean top-of-atmosphere net energy flux for HAT-P-11b, HD 189733b, HD 209458b, and WASP-17b levels off at 0.6, 5, 8, and 23 $kW\,m^{-2}$, respectively, indicating a net inward energy flux equal to less than 5 per cent of the corresponding incoming energy flux, and changes by less than 1 per cent over the last 200 d.

The total mass of chemical species evolves differently within each atmospheric layer. It increases if a species is produced within or advected into a layer, and decreases if a species is destroyed within or advected from a layer. Depending on the time-scale of processes driving the change in the total species mass, different layers require a different amount of time to reach steady state. To see which layers approach or are at steady state, we integrated the mass of chemical species within two arbitrary chosen pressure ranges ($1 \times 10^2 – 1 \times 10^4$ Pa and $1 \times 10^2 – 1 \times 10^5$ Pa) and over the entire model domain ($1 \times 10^2 – 1 \times 10^7$ Pa). We performed this calculation for both,

equilibrium and kinetics, simulations, and as expected, found larger changes in the total species mass in the kinetics simulations discussed in detail below. However, the HAT-P-11b equilibrium simulation was an exception, where the pressure-temperature structure has changed enough on its own to cause the same (1.3 per cent) increase in the total mass of HCN within $1 \times 10^2 – 1 \times 10^4$ Pa as in the HAT-P-11b kinetics simulation.

The domain-total mass of chemical species changes little over time because the majority of atmospheric mass is located at high pressure levels (in a regime controlled by chemical equilibrium), making the contribution of the low pressure levels (under potential chemical disequilibrium) to the total relatively small. When deep atmospheric layers are excluded (by integrating mass over a narrower pressure range, e.g. $1 \times 10^2 – 1 \times 10^5$ Pa), the total species mass changes more noticeably, especially in the kinetics simulations. For HAT-P-11b, NH_3 and HCN increase by 2.3 per cent and 1.3 per cent, respectively, from their initial total mass, and for HD 189733b, CH_4, NH_3, and HCN increase by 1.6 per cent, 4.5 per cent, and 4.8 per cent, respectively, from their initial total mass. When an even thinner atmospheric layer is considered ($1 \times 10^2 – 1 \times 10^4$ Pa), its total species mass evolves differently from its equivalent for a thicker layer, and might reach a different stable mass. For HAT-P-11b, NH_3 and HCN increase by a similar amount in this thinner layer relative to a thicker layer. However, for HD 189733b, CH_4, NH_3, and HCN increase by 1.3 per cent, 3.6 per cent, and 3.6 per cent, respectively, which is less than their corresponding increases in a thicker layer, and for HD 209458b, CH_4 increases by 4.6 per cent, which is more than its corresponding increase (less than 1 per cent) in a thicker layer. These examples illustrate the difference in evolution of the total mass of chemical species in various atmospheric layers. We
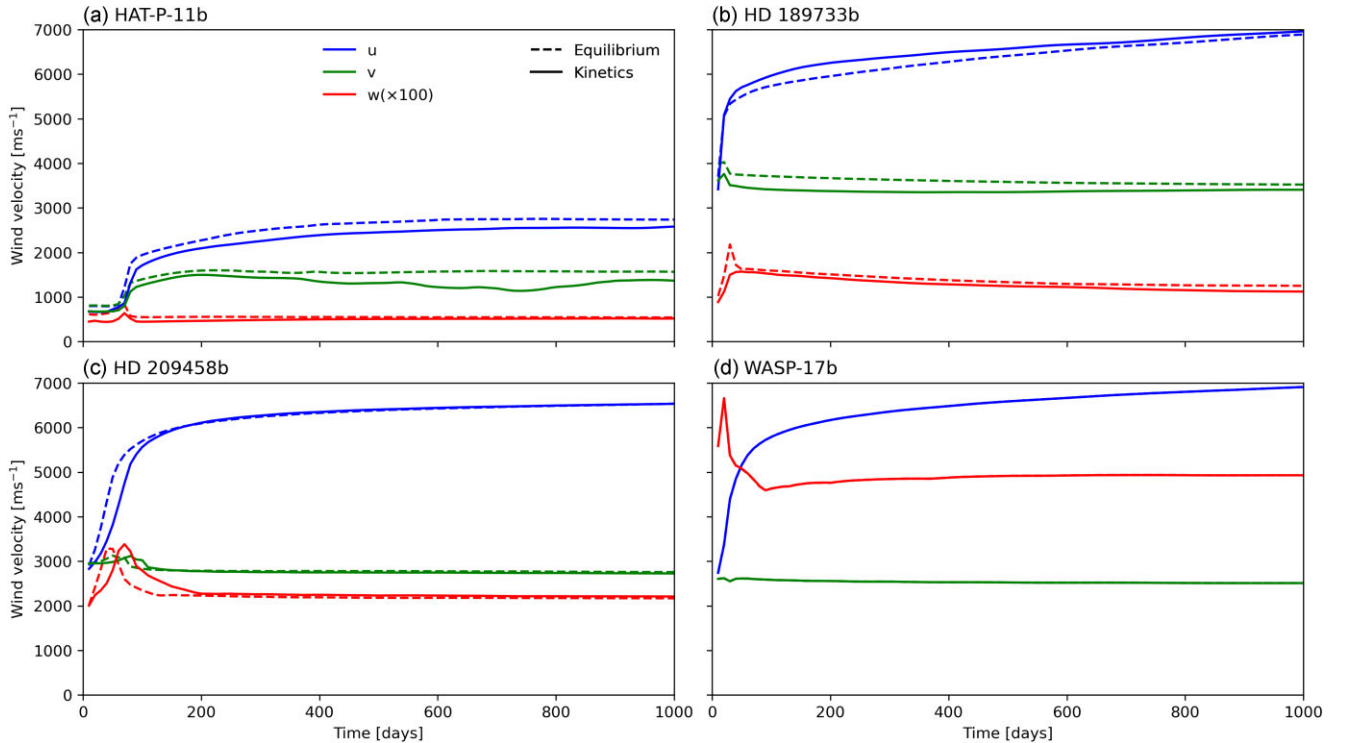
Figure B1. Evolution of the global maximum of the zonal (blue), meridional (green), and vertical (red) components of the wind velocity from the equilibrium (dashed) and kinetics (solid) simulations of HAT-P-11b (a), HD 189733b (b), HD 209458b (c), and WASP-17b (d). Note that the vertical wind velocity is scaled by a factor of a 100.
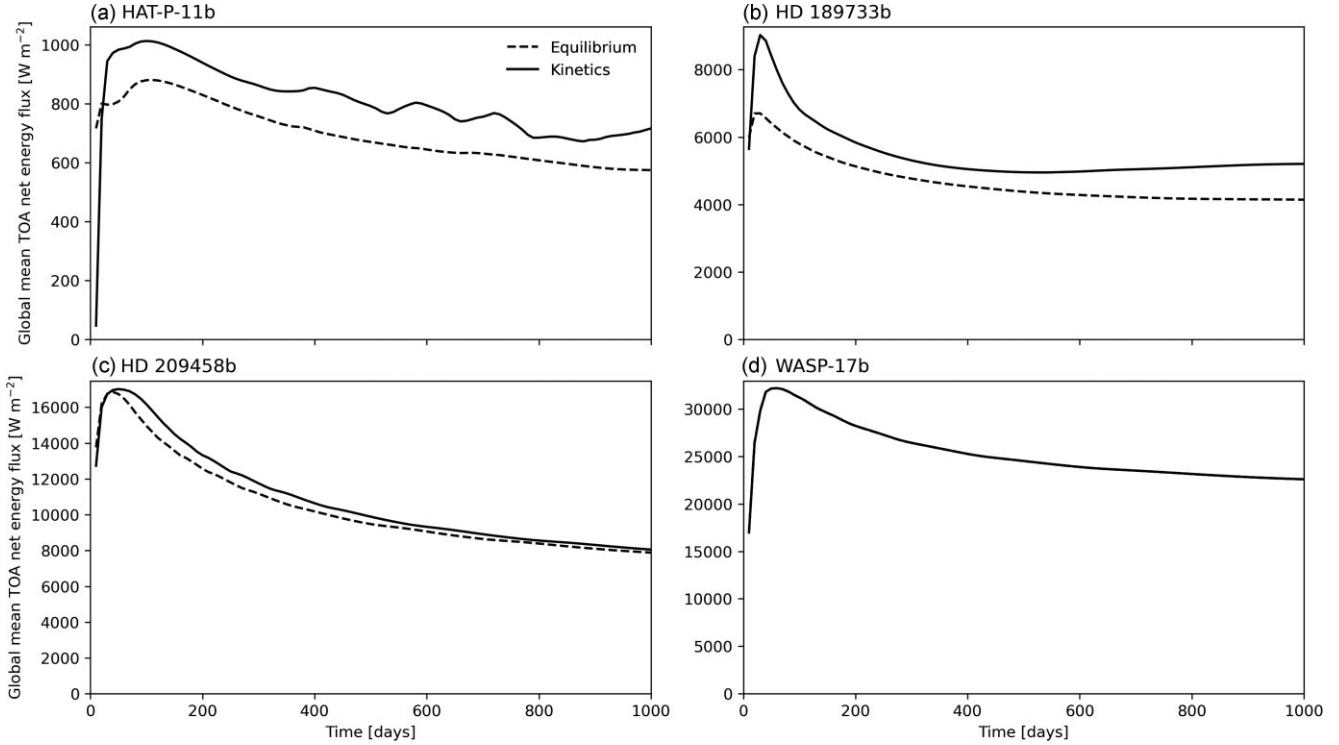
Figure B2. Evolution of the global mean top-of-atmosphere net energy flux from the equilibrium (dashed) and kinetics (solid) simulations of HAT-P-11b (a), HD 189733b (b), HD 209458b (c), and WASP-17b (d).
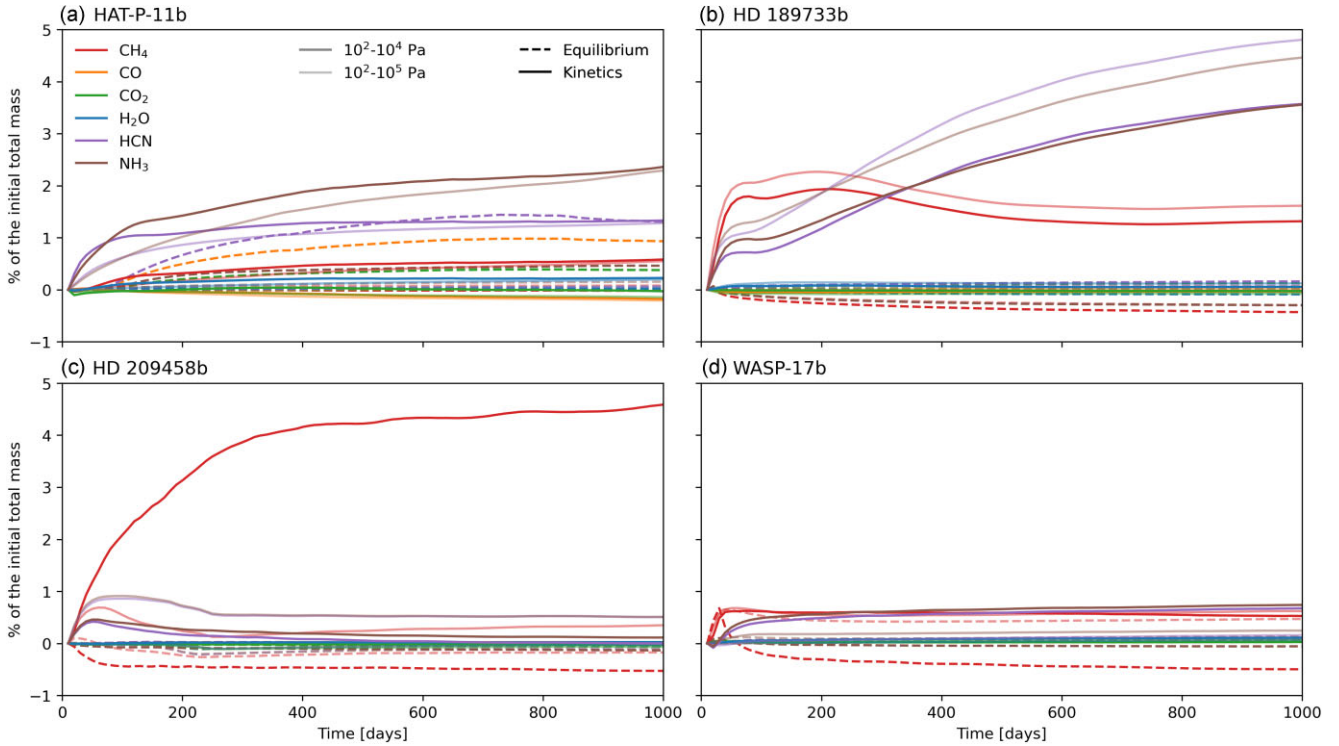

Figure B3. Evolution of the total mass of CH_4, CO, CO_2, H_2O, HCN, and NH_3 within 1×10^2–1×10^4 Pa and 1×10^2–1×10^5 Pa from the equilibrium (dashed) and kinetics (solid) simulations of HAT-P-11b (a), HD 189733b (b), HD 209458b (c), and WASP-17b (d).

recommend checking this evolution for atmospheric layers of interest when discussing the proximity of the model simulation to a chemical steady state.

Given the results for the dynamical and radiative metrics mentioned above, and the fact that in all our simulations the total mass of major opacity sources in the atmospheric layer bound by 1×10^2–

1×10^5 Pa changes by less than 1 per cent over the last 200 d, we conclude that this atmospheric layer has reached the dynamical, radiative, and chemical pseudo-steady state.

APPENDIX C: ADDITIONAL FIGURES
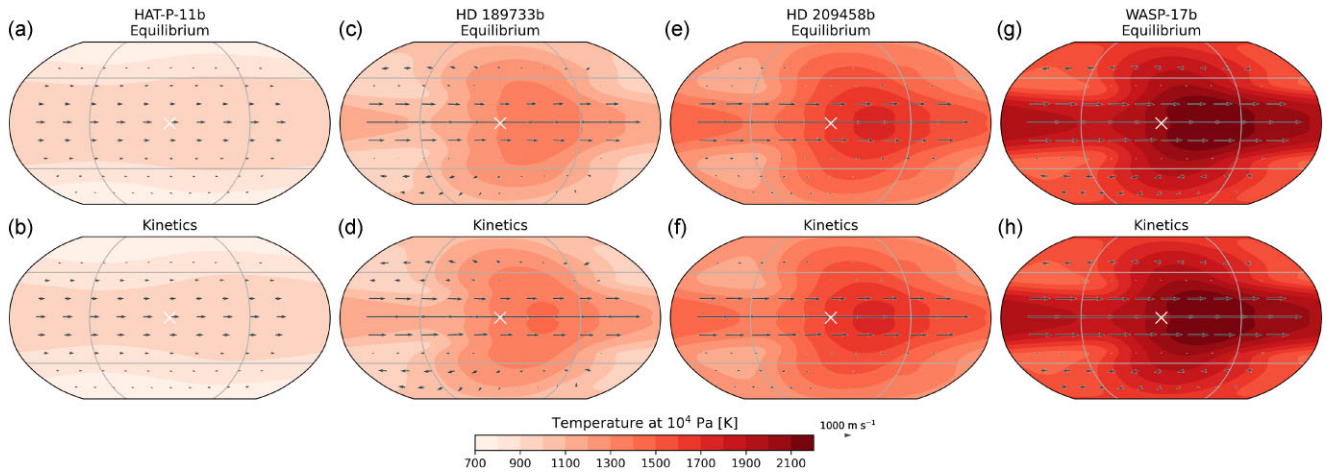
Figure C1. Temperature and horizontal winds at the 1×10^4 Pa pressure level. White cross denotes the substellar point. Grey grid lines show $\pm 45°$ latitude and $90°$ and $270°$ longitude.
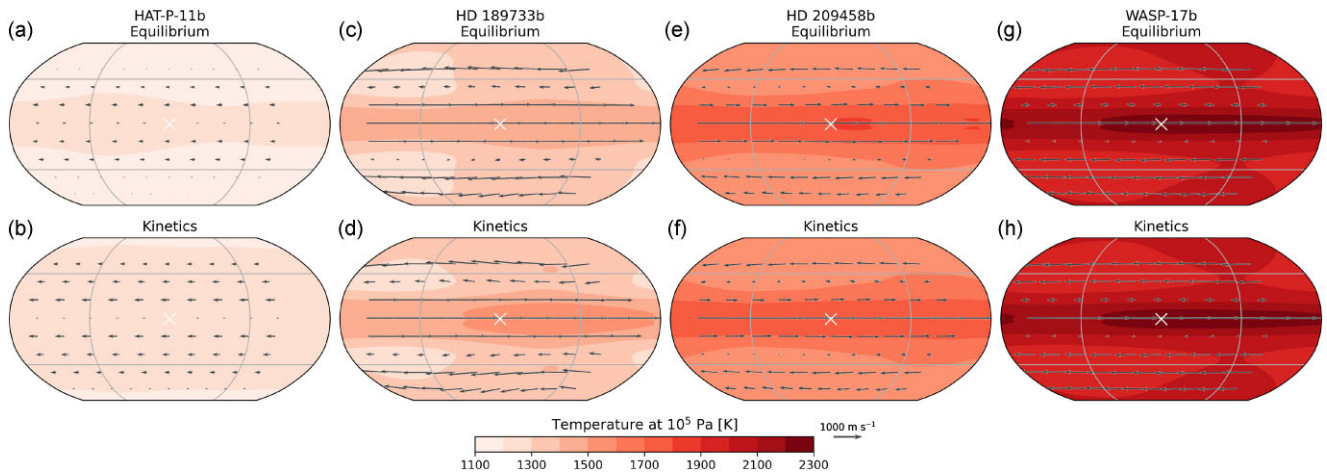
Figure C2. As in Fig. C1 but for the 1×10^5 Pa pressure level.
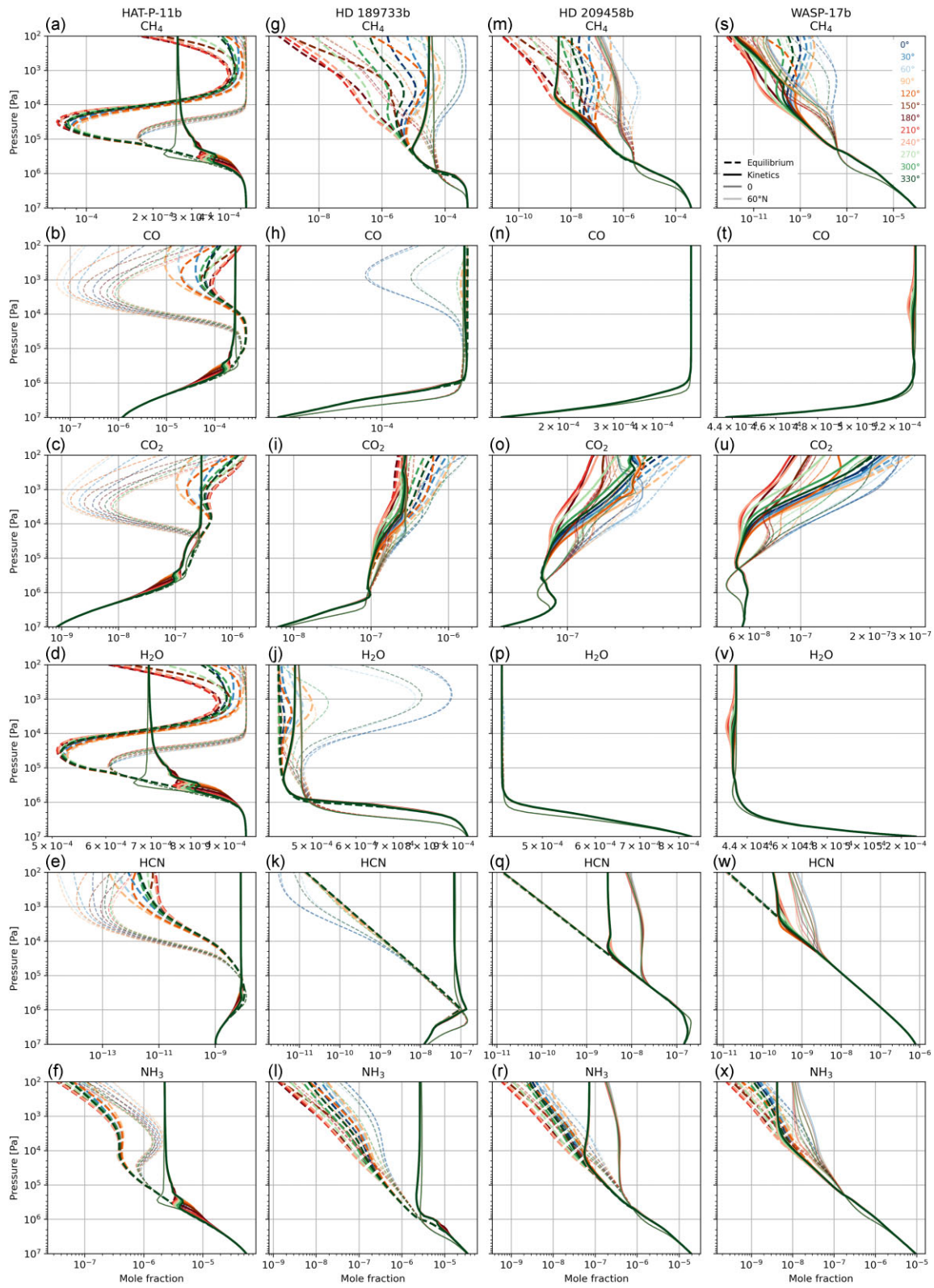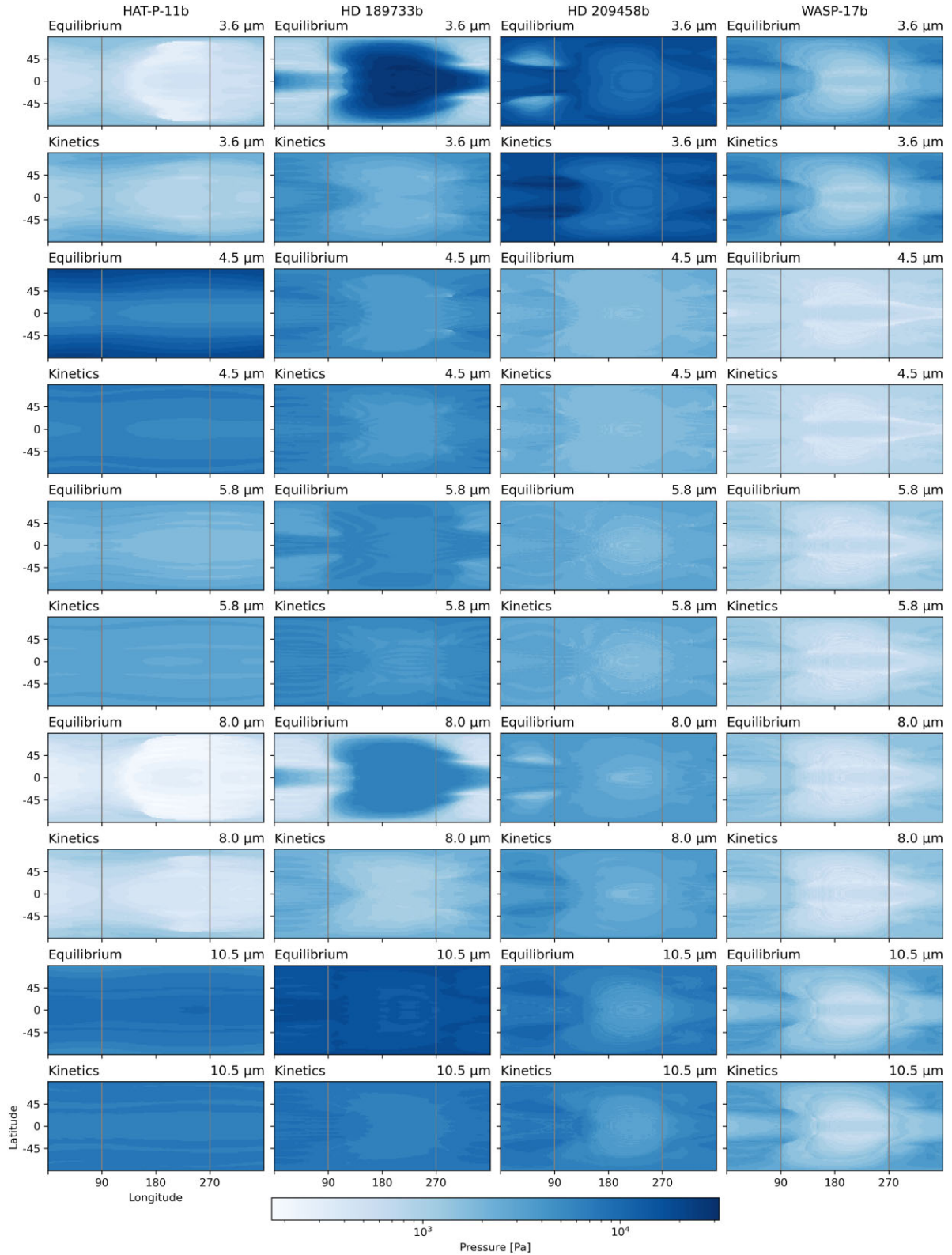
Figure C3. As in Fig. 3 but with different X-axes.

Figure C4. Pressure at a pressure level of the photosphere in individual spectral bands closest to 3.6, 4.5, 5.8, 8.0, and 10.5 μm associated with the peaks in absorption by CH_4, CO, H_2O, CH_4, and NH_3, respectively, for the equilibrium and kinetics simulations of HAT-P-11b (first column), HD 189733b (second column), HD 209458b (third column), and WASP-17b (fourth column). The substellar point is located at 180° latitude. Grey grid lines show 90° and 270° longitude.
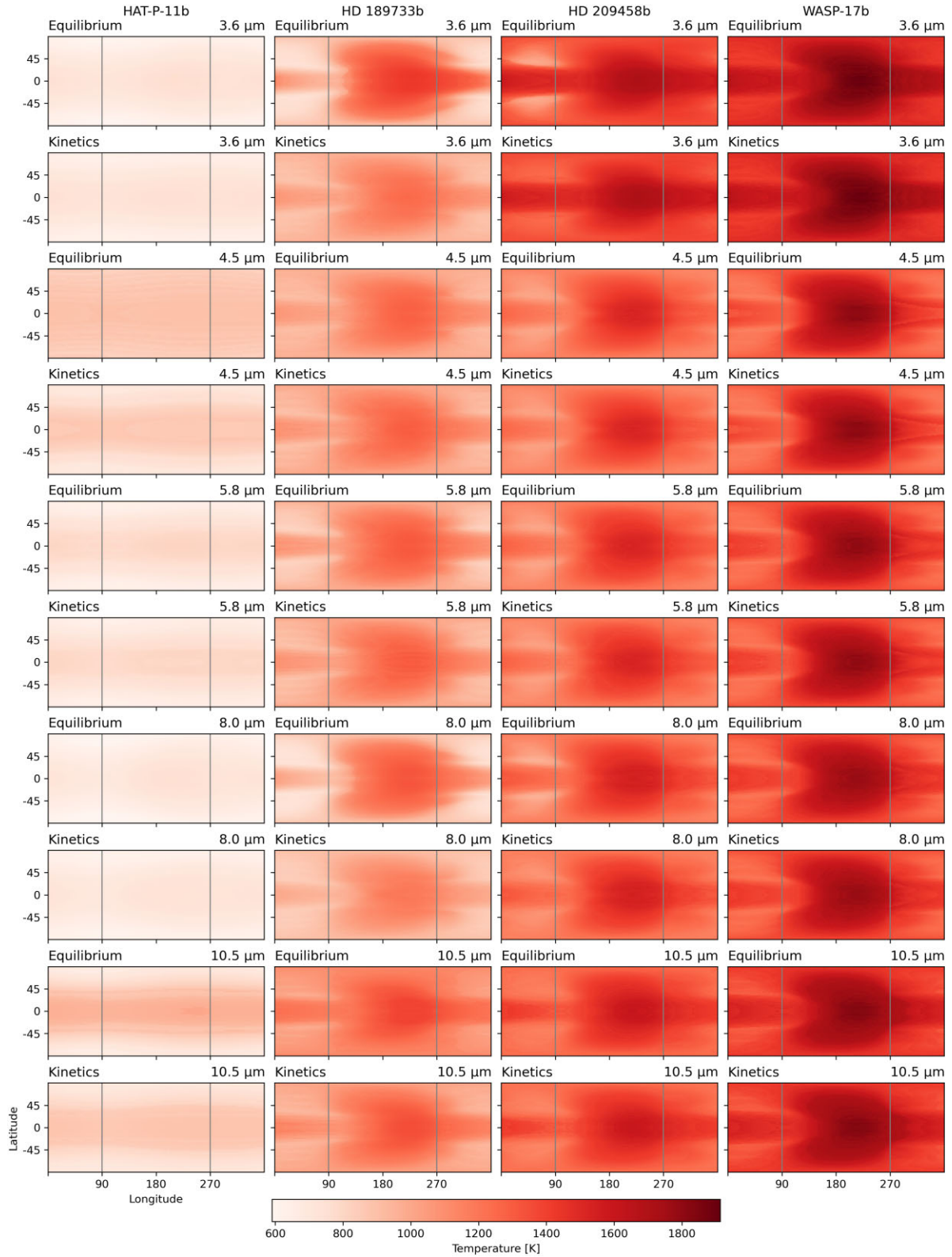
Figure C5. As in Fig. C4 but for temperature.
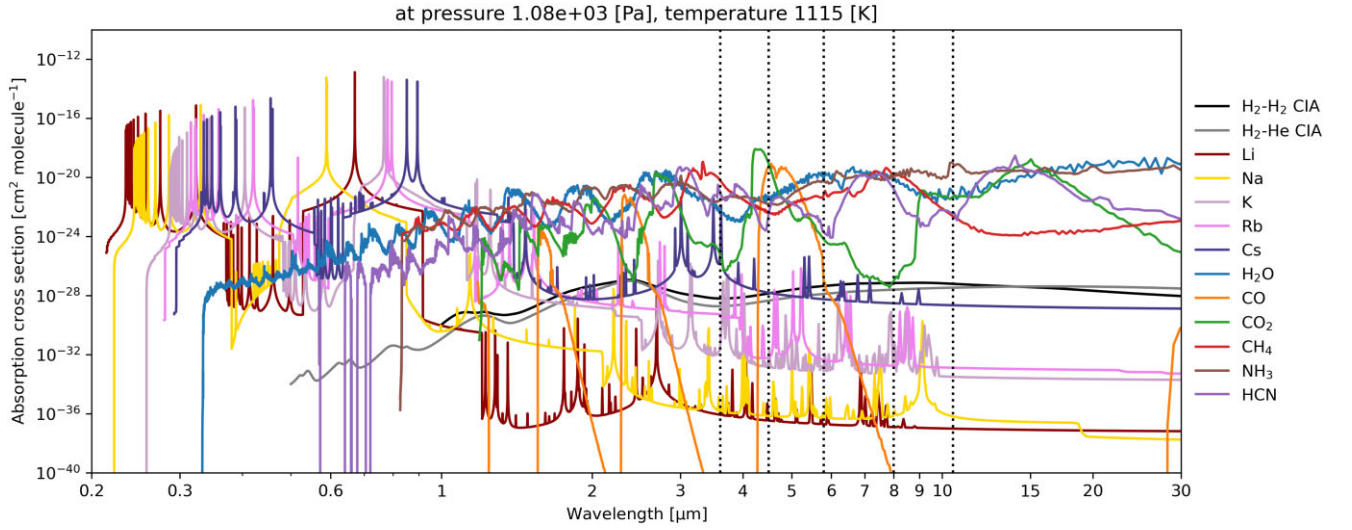
Figure C6. Absolute absorption cross-sections of the opacity sources included into our UM simulations in this study (H_2-H_2 CIA, H_2-He CIA, Li, Na, K, Rb, Cs, H_2O, CO, CO_2, CH_4, NH_3, and HCN) at 1.08×10^3 Pa and 1115 K calculated from the SOCRATES 5000 band spectral files following the methodology of Goyal et al. (2020). Black dotted vertical lines highlight wavelengths corresponding to the centres of the *Spitzer*/IRAC channels and 10.5 μm. These absorption cross-sections are not exact but are relevant for the 10.5 μm photosphere pressures and temperatures in HD 189733b kinetics simulation.
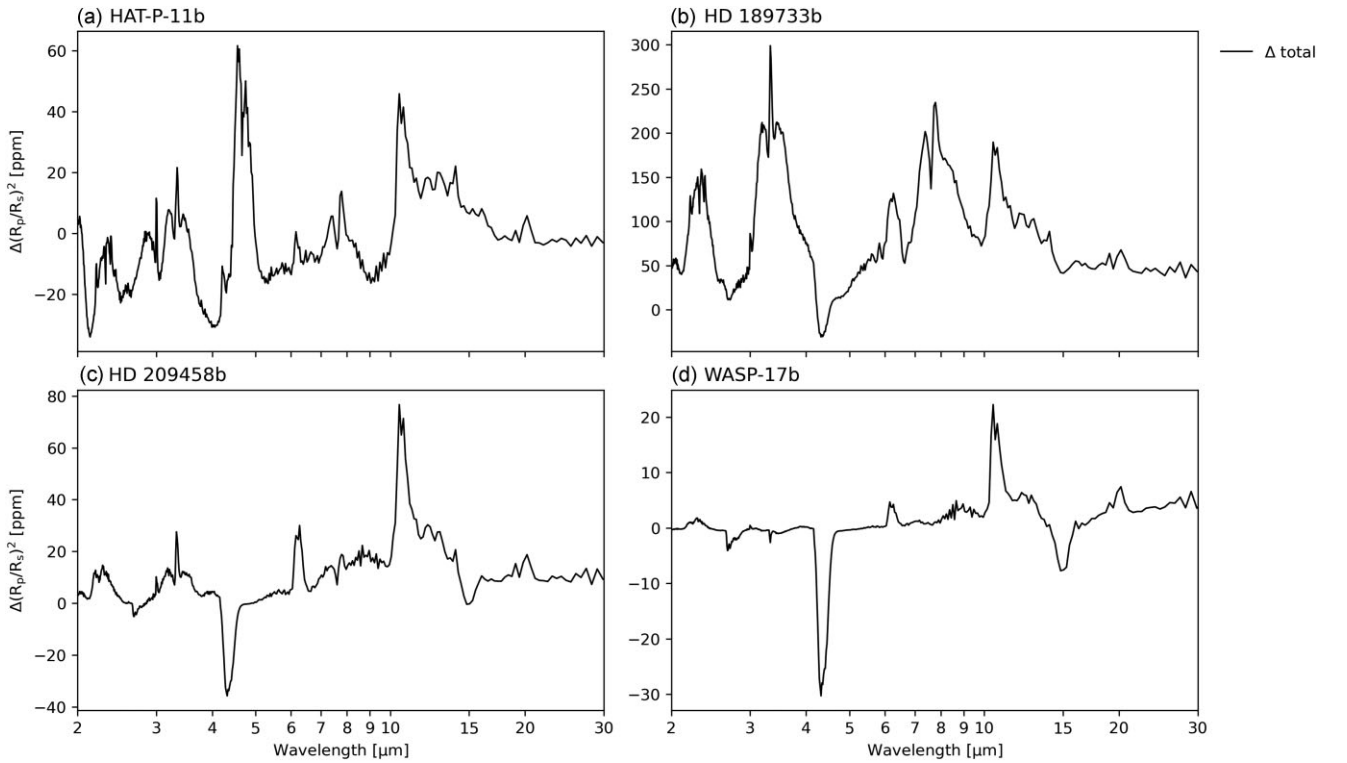
Figure C7. As in Fig. 5 but differences between simulations (kinetics minus equilibrium).

This paper has been typeset from a TeX/LaTeX file prepared by the author.